Digital Comprehensive Summaries of Uppsala Dissertations from the Faculty of Science and Technology 2399

Porous Materials and Their Cellulose-Based Composites

Synthesis, Nanoengineering, and Applications

XUEYING KONG

ACTA UNIVERSITATIS
UPSALIENSIS
2024

ISSN 1651-6214
ISBN 978-91-513-2118-9
urn:nbn:se:uu:diva-526314

UPPSALA
UNIVERSITET

Dissertation presented at Uppsala University to be publicly examined in Häggsalen (Å10132), Ångströmlaboratoriet Lägerhyddsvägen 1, Uppsala, Friday, 31 May 2024 at 13:15 for the degree of Doctor of Philosophy. The examination will be conducted in English. Faculty examiner: Professor Arne Thomas (Technical University Berlin, Institute of Chemistry).

Abstract

Kong, X. 2024. Porous Materials and Their Cellulose-Based Composites. Synthesis, Nanoengineering, and Applications. *Digital Comprehensive Summaries of Uppsala Dissertations from the Faculty of Science and Technology* 2399. 81 pp. Uppsala: Acta Universitatis Upsaliensis. ISBN 978-91-513-2118-9.

Porous materials, such as porous carbons (PCs), metal-organic frameworks (MOFs), and covalent organic frameworks (COFs), show considerable potential across various fields because of their rich microporous and mesoporous structures and large surface areas, yet they grapple with challenges like environmentally unfriendly fabrication methods and poor processability. In this thesis, we investigated environmentally friendly fabrication methods for porous materials, nanoengineering techniques for processing these materials, and their potential applications.

Cladophora cellulose (CC), a naturally abundant biopolymer, was used to prepare PC via a one-step physical carbonization/activation method without using any corrosive activation agents. The obtained CC-derived PC (CPC) showed a high specific surface area (507.2 m^2 g^{-1}) and rich microporous structure. Additionally, we introduced a simple and environmentally friendly method for synthesizing imine-linked COFs at room temperature using water as the solvent. The method involves a key step in which aldehyde monomers are pre-activated by acetic acid, which promotes the aldehyde monomers to dissolve in water, enhancing their reactivity with amine monomers, and ensuring the formation of crystalline COFs. Consequently, we synthesized 16 distinct imine-linked COFs with high crystallinity and specific surface areas.

Furthermore, this thesis focusses on improving the poor processability of these materials caused by the infusible and insoluble nature of their powders. The poor processability of these porous materials makes them difficult to process into desired structures and shapes. Here, we introduce two nanoengineering methods: i) Interweaving porous materials with CC nanofibers (CNFs) to form CNF-porous material aqueous solutions; and ii) Interfacial synthesis of porous materials on the surface of carboxylated CNFs to form CNF@porous materials with nanofiber structures in aqueous solutions. The obtained composite suspensions can be fabricated into freestanding and flexible composite nanopapers via a vacuum filtration and drying process. In addition, they can be processed into freestanding aerogels through a freeze-drying process. Consequently, we have successfully prepared freestanding and flexible CC-CPC nanopapers and CC-CPC aerogels, c-CNT@COF/CNT/CNF nanopapers (c-CNT: carboxylated carbon nanotube), CNF@MOF nanopapers, and CNF@COF nanopapers and demonstrated their potential in various applications, from efficient CO_2 capture and organic pollutant removal to advanced energy storage and solar vapor generation.

In summary, we used environmentally friendly methods to synthesize PC and imine-linked COFs, circumventing the need for corrosive chemical agents and toxic organic solvents, respectively. Furthermore, by combining CNFs with porous materials, we successfully created freestanding and flexible nanopapers and aerogels, thereby addressing the issue of poor processability associated with porous materials.

Keywords: Porous Carbon, Covalent Organic Frameworks, Metal-Organic Frameworks, Cladophora Cellulose Nanofibers, Cellulose-based Flexible Nanocomposites

Xueying Kong, Department of Materials Science and Engineering, Nanotechnology and Functional Materials, Box 35, Uppsala University, SE-751 03 Uppsala, Sweden.

ISSN 1651-6214
ISBN 978-91-513-2118-9
URN urn:nbn:se:uu:diva-526314 (http://urn.kb.se/resolve?urn=urn:nbn:se:uu:diva-526314)

To make each day count.

List of Papers

This thesis is based on the following papers, which are referred to in the text by their Roman numerals.

I. **Kong X.,** Zhou S., Strømme M., Xu C. (2022) All-Cellulose-Based Freestanding Porous Carbon Nanocomposites and Their Versatile Applications. *Composites Part B: Engineering,* 232: 109602.

II. Zhou S., **Kong X.,** Strømme M., Xu C. (2022) Efficient Solar Thermal Energy Conversion and Utilization by a Film of Conductive Metal–Organic Framework Layered on Nanocellulose. *ACS Materials Letters*, 4(6): 1058–1064.

III. **Kong X.,** Zhou S., Strømme M., Xu C. (2021) Redox Active Covalent Organic Framework-Based Conductive Nanofibers for Flexible Energy Storage Device. *Carbon*, 171: 248–256.

IV. **Kong X.,** Wu Z., Strømme M., Xu C. (2024) Ambient Aqueous Synthesis of Imine-Linked Covalent Organic Frameworks (COFs) and Fabrication of Freestanding Cellulose Nanofiber@COF Nanopapers. *Journal of the American Chemical Society*, 146 (1): 742–751.

Contributions to the papers

I. I conceived the ideas, designed and conducted the experiments, analyzed the data, discussed the results, and wrote the manuscript.

II. I synthesized the materials and conducted the spectral characterization, discussed the results, and revised the manuscript.

III. I conceived the ideas, designed and conducted the experiments, analyzed the data, discussed the results, and wrote the manuscript.

IV. I conceived the ideas, designed and conducted the experiments, analyzed the data, discussed the results, and wrote the manuscript.

Other contributions

Publications:

I. Afewerki S., Wang X., Ruiz-Esparza G. U., Tai C. W., **Kong X.,** Zhou S., Welch K., Huang P., Bengtsson R., Xu C., Strømme M. (2020) Combined Catalysis for Engineering Bioinspired, Lignin-Based, Long-Lasting, Adhesive, Self-Mending, Antimicrobial Hydrogels. *ACS Nano,* 14(12): 17004–17017.

Participation in conferences:

Kong X., Wu Z., Strømme M., Xu C. Aqueous Synthesis and Engineering of Imine-Linked Covalent Organic Frameworks. Sorption, Transport and Catalysis in Metal-Organic Frameworks 2023, (Uppsala Sweden), 2023. Poster presentation.

Abbreviations

AC	Activated Carbon
BET	Brunauer–Emmett–Teller
CC	*Cladophora* Cellulose
CPC	*Cladophora* Cellulose Derived Porous Carbon
CNF	*Cladophora* Cellulose Nanofiber
CNT	Carbon Nanotube
c-CNT	Carboxylated Carbon Nanotube
COF	Covalent Organic Framework
HKUST	Hong Kong University of Science and Technology
IR	Infrared
MOF	Metal-Organic Framework
MIL	Material Institute Lavoisier
PC	Porous Carbon
PTSA	p-Toluene Sulfonic Acid
SEM	Scanning Electron Microscopy
TEM	Transmission Electron Microscope
TGA	Thermogravimetric Analyser
UIO	University of Oslo
XPS	X–ray Photoelectron Spectroscopy
XRD	X–ray Diffraction
ZIF	Zeolitic Imidazolate Framework

Contents

1. Introduction

1.1 Porous Materials

Porous structures are present in a variety of materials, ranging from classical inorganic materials to organic and hybrid framework solids. In 1985, the International Union of Pure and Applied Chemistry classified pores by their sizes: pore sizes of 2 nm and below are called micropores, those in the range of 2 nm to 50 nm are denoted mesopores, and those above 50 nm are macropores.[1] The pore properties, including size, shape, and volume, significantly influence on the performance of their particular applications. Typical porous materials, such as porous carbons (PCs), metal-organic frameworks (MOFs), and covalent organic frameworks (COFs) with microporous and mesoporous architectures, have been identified as ideal candidates for applications, such as: adsorption,[2] catalysis,[3] separation,[4] purification,[5] and energy storage and conversion.[6]

1.2 Porous Carbons (PCs)

PCs have attracted significant attention due to their remarkable properties, including high specific surface areas, hierarchical porosity, high thermal conductivity, high chemical stability, and good electrical conductivity.[7-10] These properties enable PCs to be applied in different applications, such as adsorption,[11] purification,[12] and energy storage and conversion.[13] Traditionally, PCs are obtained from carbonization and activation processes using different precursors (Figure 1). Typically, precursors undergo pyrolysis at temperatures ranging from 400 to 1000 °C in an inert atmosphere. Subsequently, the resulting solid carbons, known as coal char or biochar, typically have a nonporous structure. To obtain porous structures, coal char or biochar have to be activated using physical activation agents (steam, CO_2, or other gases) or chemical activation agents (KOH, NaOH, Na_2CO_3, $ZnCl_2$, H_3PO_4 or other chemicals).[13-14]

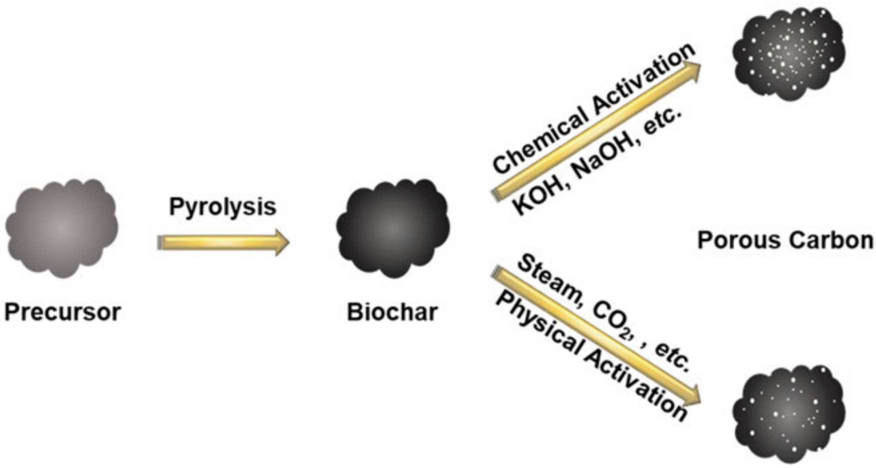

Figure 1 The fabrication of porous carbon.

Chemical agents activate char at temperatures ranging from 400 to 900 °C.[15-17] The PC produced through the chemical activation strategy shows a high specific surface area (ranging from 500–3600 $m^2\ g^{-1}$). However, high activation agent/char ratios (ranging from 1 to 10) are required in the chemical activation process. The utilization of excessive chemical agents increases production cost and limits the development of the chemical activation method in the large-scale production of PCs. More importantly, these chemical agents, especially KOH and NaOH, are highly corrosive substances, which are harmful to the environment.

Physical agents, such as steam and CO_2, react with char at temperatures ranging from 600 to 1200 °C.[18-20] Compared to chemical activation strategy, physical activation usually requires higher activation temperatures and longer activation times. Additionally, the PC produced exhibits smaller pore sizes, and lower specific surface areas (up to 1500 $m^2\ g^{-1}$) than that obtained from chemical activation. However, these physical activation strategies do not involve the use of corrosive agents, making them more environmentally friendly. Therefore, physical activation methods deemed suitable for the practical production of PCs.

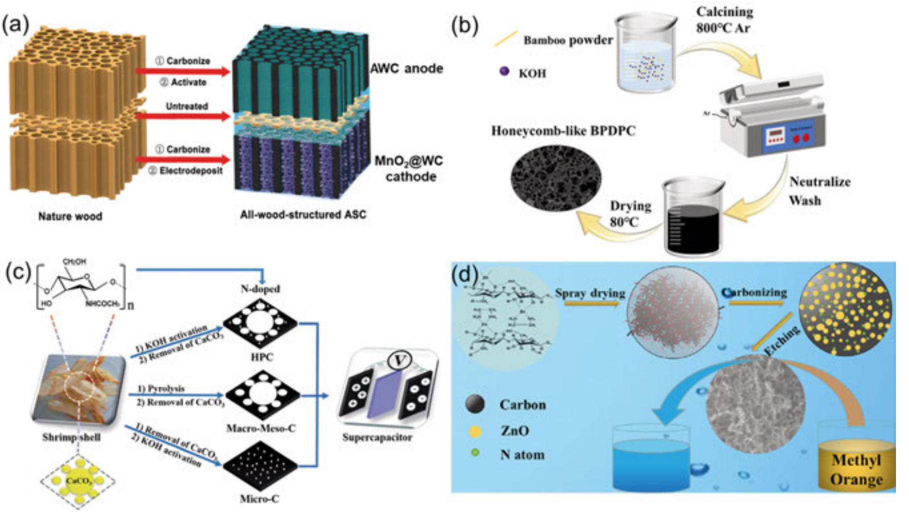

Figure 2 (a) Graphical illustration of the design concept and construction process of the all-wood-structured supercapacitor. AWC stands for "activated wood carbon" and WC stands for "wood carbon".[21] Copyright (2017), published by Royal Society of Chemistry. (b) Schematic diagram of the synthesis process of bamboo powders-derived porous carbon (BPDPC).[22] Copyright (2023), with permission from Elsevier. (c) Synthesis schematic of hierarchical porous carbon (HPC), macro–meso-carbon and micro-carbon from shrimp shell.[23] Copyright (2016), published by Royal Society of Chemistry. (d) Synthesis schematic of nitrogen-doped porous carbons (NPCs) derived from waste-cellulose and the illustration of NPCs for removing methyl orange (MO) from water.[24] Copyright (2019), with permission from Elsevier.

A variety of precursors, such as polymers,[8] MOFs,[25] and biomass,[26] have been used to fabricate PCs. Among these, biomass precursors,[11] including wood, bamboo, algae, and shrimp shells, are considered the most promising materials because they are abundant, cheap, readily available, and renewable. For example, Hu et al. reported a synthesis method for activated carbon derived from natural basswood blocks (Figure 2a).[21] The process for preparing activated carbon involves two steps: carbonization under an argon atmosphere and activation in a CO_2 atmosphere at high temperatures. This activated carbon exhibited a hierarchical porous structure, ensuring efficient electrolyte transfer in electrochemical energy storage devices. When used as the anode for an all-wood-structured asymmetric supercapacitor, the supercapacitor showed a high energy density (1.6 mWh cm^{-2}) at the maximum power density (24 W cm^{-2}). Zhou et al. reported a synthesis strategy for honeycomb-like bamboo powder-derived porous carbon (BPDPC), involving carbonization and chemical activation steps (Figure 2b).[22] The resulting honeycomb-like BPDPC was treated with HCl to remove impurities and then washed with DI water. Subsequently, the purified honeycomb-like BPDPC was used as a microwave absorber and shows a maximum adsorption bandwidth of 4.76 GHZ and a minimum reflection loss of −40.99 dB at a low filler loading of 5 wt%. Wu et al.

have reported nitrogen-doped hierarchical porous carbon (HPC) prepared from shrimp shells using a KOH activation and carbonization strategy (Figure 2c).[23] The obtained nitrogen-doped HPC showed an abundance of micropores, mesopores and interconnected macropores, and exhibited a high electrochemical capacitance (348 F g^{-1} in a 6 M KOH electrolyte). Zhao et al. developed a nitrogen-doped PC derived from waste cellulose fibers via a series of complex procedures (Figure 2d), involving spray drying, pyrolysis, and nitric acid washing to remove the porogen (ZnO).[24] The obtained nitrogen-doped PC exhibited a high specific surface area (1259.4 m^2 g^{-1}) and pore volume (2.7 cm^3 g^{-1}) and demonstrated a high adsorption capacity for methyl orange (337.8 mg g^{-1}) in water .

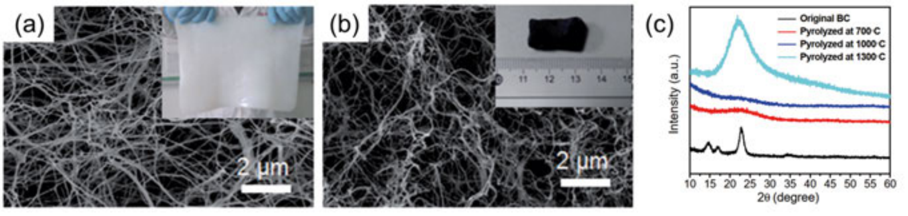

Figure 3 (a, b) Scanning electron microscopy (SEM) images of the bacterial cellulose aerogel (a) and the carbon nanofiber aerogel treated at 1300°C (b). The insets in (a) and (b) show the photographs of the bacterial cellulose pellicle and the carbon nanofiber aerogel prepared by pyrolysis at 1300°C. (c) X–ray diffraction (XRD) patterns of the bacterial cellulose aerogel and the carbon nanofiber aerogels prepared by pyrolysis at different temperatures.[2] Copyright (2013), published by WILEY-VCH Verlag GmbH & Co. KGaA, Weinheim.

Although the above methods used cheap and renewable biomass precursor to prepare PCs, their complex procedure and the use of corrosive chemicals increase production costs and pose risks to the environment, limiting their practical applicability. Therefore, a less corrosive and more cost-effective method for preparing PCs from biomass is needed. To this end, Yu et al. fabricated a PC with microporous and mesoporous structures derived from bacterial cellulose with high crystallinity using a direct pyrolysis method under an inert nitrogen atmosphere (Figure 3).[2] Bacterial cellulose consists of light elements such as C, H, and O, consequently, volatile species like H_2O, CO, and CO_2 are produced during their pyrolysis. These volatile species serve as porogens, facilitating the formation of porous structures in the resulting carbon materials. Nevertheless, the direct pyrolysis method is not suitable for all cellulose materials. Some cellulose derived carbon materials are pyrolyzed into coal char, requiring an additional activation process to generate porous structures, which could be associated with their low crystallinity.[9]

1.3 Metal-Organic Frameworks (MOFs)

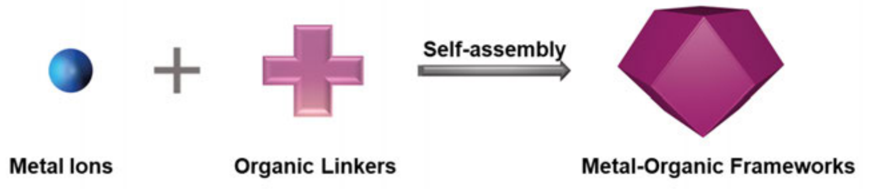

Figure 4 Formation of metal-organic frameworks.

MOFs are a new type of porous material formed by the self-assembly of metal ions or clusters with organic ligands (Figure 4). MOFs exhibit diverse topological features owing to the diversity of metal ions, organic ligands, and their various combinations.[27] Various synthetic methods have been employed to fabricate MOFs, including solvothermal,[28] hydrothermal,[29] microwave,[30] sonication,[31] and mechanical grinding-assisted methods.[32] Many MOFs possess excellent properties, such as high porosity (up to 90% free volume), ultra-high specific surface areas (up to 7000 $m^2 g^{-1}$), and low density (as low as 0.13 g cm^{-3}).[33] Owing to these properties, MOFs have been widely used in various applications , such as gas storage and separation,[34] catalysis,[35] drug delivery,[36] energy storage and conversion,[37] proton conduction,[38] and sensing.[39]

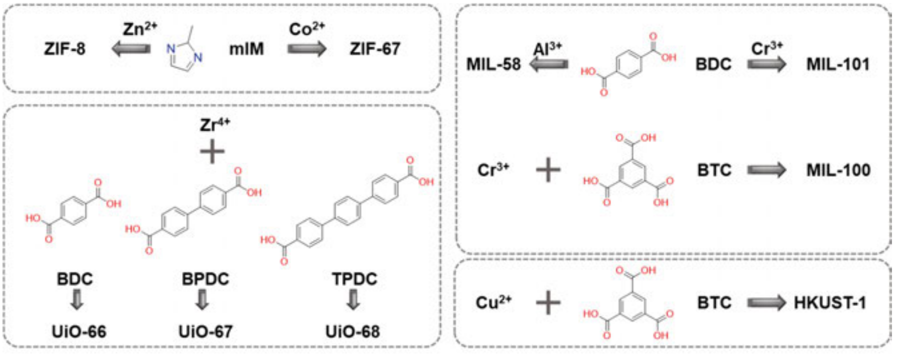

Figure 5 Formations of ZIF-67, ZIF-8, UiO-66, UiO-67, UiO-68, MIL-58, MIL-101, MIL-100, and HKUST-1.

MOFs can be classified based on the different functional groups of the organic ligands (Figures 5 and 6), typical organic ligands include: azolates (such as imidazolates, pyrazolates, triazolates, and tetrazolates), carboxylate-based ligands, hydroxyl-based ligands, amine-based ligands, and sulfhydryl-based ligands. The ZIFs series (Zeolitic Imidazolate Frameworks) including well-known ZIF-8, and ZIF-67, are constructed with imidazolate linkers and low-valent transition metal ions, such as Zn^{2+}, and Co^{2+}. The MIL series (Material Institut Lavoisier) including MIL-53, MIL-100, and MIL-101, are constructed with carboxylate-based ligands and high-valent metal ions, such as Al^{3+}, Fe^{3+}, and Cr^{3+}. The UiO series (University of Oslo) including UiO-66, UiO-67, and UiO-68, are constructed with carboxylate-based ligands and high-valent metal ions (Zr^{4+}). The HKUST-1 (Hong Kong University of Science and Technology) is constructed with carboxylate-based ligands and low-valent transition metal ions (Cu^{2+}).

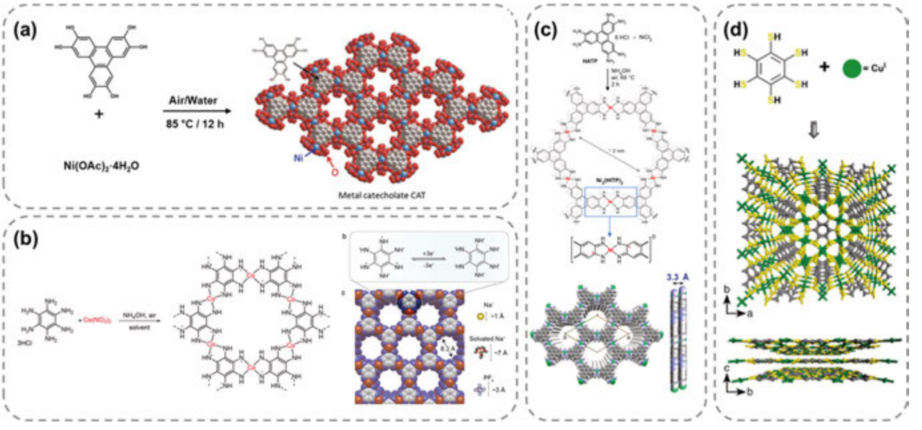

Figure 6 Structures of (a) Ni-HHTP (Ni-CAT).[40] Copyright (2012), published by American Chemical Society. (b) Co-HAB.[41] Copyright (2018), published by American Chemical Society. (c) Ni-HITP.[29] Copyright (2014), published by American Chemical Society. (d) Cu-BHT.[42] Copyright (2023), published by American Chemical Society.

Most MOFs are insulators because of their large band gaps and lack of charge carriers, limiting their applications in fields that require electrical conductivity. Through rational design or post-synthetic modification of organic bridging ligands, a variety of functional groups can be introduced into the framework of MOF to regulate its physical/chemical microenvironment to obtain special properties such as high electrical conductivity, and thereby improve the performance for electrochemical applications.[43] By this strategy, various conductive MOFs (c-MOFs) have been designed and fabricated. For instance, Yaghi et al. synthesized Co-HHTP, Ni-HHTP, and Cu-HHTP (HHTP: 2, 3, 6, 7, 10, 11-hexahydroxytriphenylene) via a hydrothermal method (Figure 6a).[40] The obtained Cu-HHTP has a conductivity of 0.21 S cm^{-1} at room temperature. Similarly, Bao et al. synthesized a new cobalt-based 2D c-MOF (Co-HAB) through a hydrothermal method (Figure 6b).[41] The obtained Co-HAB, constructed from hexaaminobenzene (HAB) and a Co (II) center, exhibits a high bulk electrical conductivity of 1.57 S cm^{-1}. Dincă et al. synthesized a novel c-MOF, Ni-HITP, assembled with 2,3,6,7,10,11-hexaiminotriphenylene (HITP) and a Ni (II) center (Figure 6c).[29] This Ni-HITP was prepared using a hydrothermal method and exhibits bulk (pellet) and surface (film) conductivity values of 2 and 40 $S\cdot cm^{-1}$, respectively. Additionally, Ameloot et al. prepared

Cu-BHT (BHT =benzenehexanothiolate) film by a solvent-free chemical vapor deposition method (Figure 6d).[42] The fabricated Cu-BHT film, with a thickness of 85 nm, has a high conductivity of 634 S cm^{-1} at 300 K.

To achieve high electrical conductivity, MOFs should allow charge transfer within their framework.[43-44] Generally, there are three primary approaches for charge transfer: the *through-bond* pathway, the through π-d conjugated plane pathway, and the *through-space* pathway. The *through-bond* pathway is achieved by the coordination bonds formed by transition metal ions (Fe^{2+}, Co^{2+}, Ni^{2+}, Cu^{2+}) and functional groups (NH_2, OH, SH) in organic linkers. These coordination bonds have orbital overlap and well-matched energy levels, thereby generating small band gaps and high charge mobilities, resulting in high electrical conductivity. The π-d conjugated plane consists of π-conjugated organic linkers and transition metal ions allow electrons to delocalize over the plane, facilitating the movement of charge across the MOF. Within MOF structures, the organic linkers engaged in π−π interactions mutually generate pathways for charge transport through space, thereby enhancing the conductivity of MOFs.

Owing to their high electrical conductivity, surface areas and porosities, c-MOFs have been successfully used in electronic sensing, energy storage and conversion. For example, Dincă et al. utilized Ni-HITP as an active electrode material to construct a electrochemical double-layer capacitor (EDLC) which showed a very high surface area-normalized capacitance of ∼18 μF cm^{-2}.[45] Bao et al. used a Ni-HAB MOFs electrode to construct a pseudocapacitors, which exhibited high volumetric capacitances of up to 760 F cm^{-3} and high areal capacitances of 20 F cm^{-2}.[46]

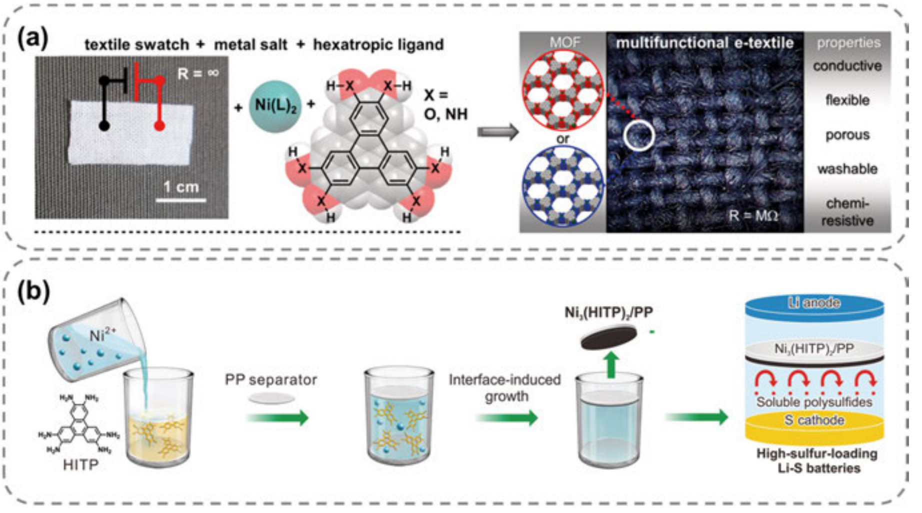

Figure 7 (a) Fabrication of MOF devices and sheet resistance of SOFT-sensor devices.[47] Copyright (2017), published by American Chemical Society. (b) Schematic illustration of the interface-induced growth of the conductive $Ni_3(HITP)_2$ modified separator for the application in Li–S batteries.[48] Copyright (2018), published by Wiley.

Although c-MOFs show excellent performances in electrochemical applications, their insoluble and infusible as powders limit their practical applications. So far, several strategies have been developed to fabricate c-MOF composites, in order to address the poor processability of c-MOF powders. For example, Mirica et al. reported multifunctional e-textiles fabricated via integrating fabrics with c-MOFs (Ni-HITP and Ni-HHTP, Figure 7a).[47] The self-organized frameworks on textiles (SOFT)-devices can be used as sensors to detect gasses (NO, H_2S, and H_2O) at ppm levels. Fang et al. fabricated a crack-free c-MOF/polypropylene (PP) membrane via an interface-induced growth strategy (Figure 7b).[48] The obtained c-MOF/PP membrane was used as a barrier layer (with a MOF mass loading of only 0.066 mg cm^{-2}) for the construction of high-performance Li–S batteries. The capacity of the Li–S batteries can reach up to 589 mAh g^{-1} at a current density of 5 C. These works have inspired us to develop new strategies to enhance the processability of c-MOF powders.

1.4 Covalent Organic Frameworks (COFs)

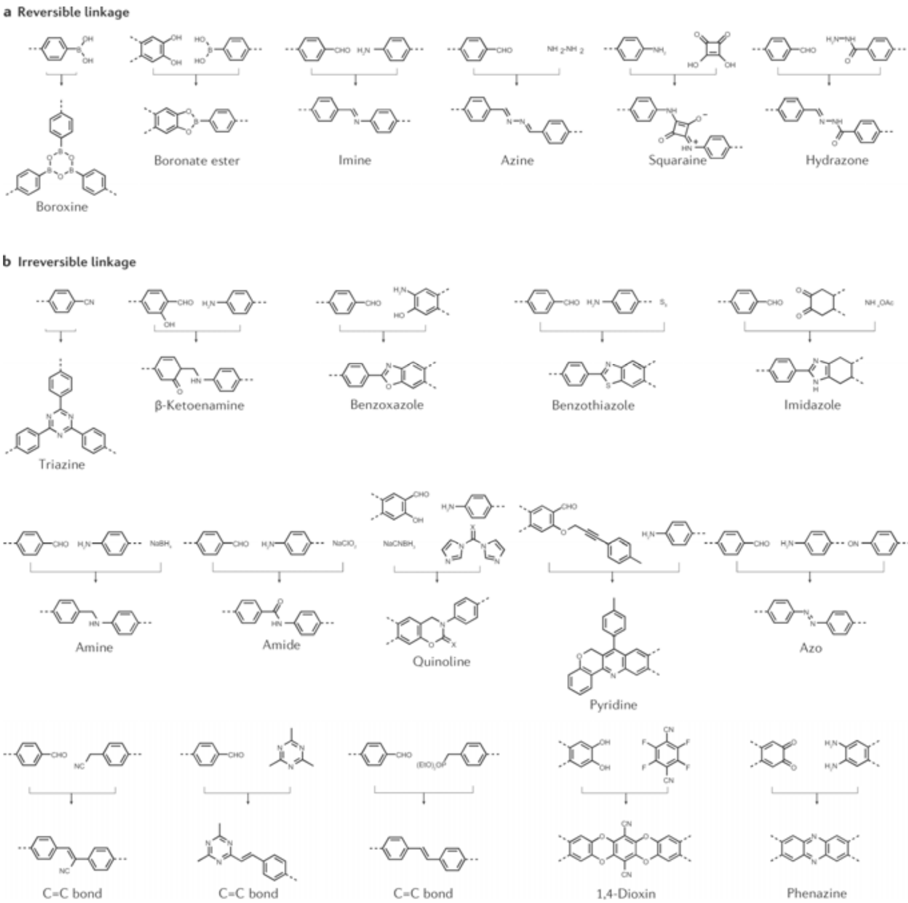

Figure 8 Reactions for linkage formation. (a) Reversible reactions. (b) Irreversible reactions.[49] Copyright (2023), published by Springer Nature.

COFs are typically porous crystalline materials formed through covalent bonds between organic building blocks.[50-52] A wide variety of COFs have been successfully synthesized by employing diverse organic building blocks. This diversity allows for the customization of COFs to exhibit various topologies, structures, functionalities, as well as different pore shapes and sizes. Given these properties, COFs have been extensively utilized in various fields, such as catalysis,[3, 53] adsorption and separation,[51, 54] luminescence,[55] sensing,[56] and energy storage and conversion.[57-58] Many distinct COFs have been designed and synthesized using reticular chemistry. COFs can be categorized according to the different covalent linkages, including: boron-containing linkages, triazine linkage, imine linkage, β-ketoenamine linkage, hydrazone and azine linkages, and others.[49] These linkages play a crucial role in determining the crystallinity and chemical stability of the COFs. Those COFs with dynamically reversible linkages often achieve high crystallinity through the self-correction of defects generated during synthetic processes. COFs with irreversible linkages usually show high chemical stability.

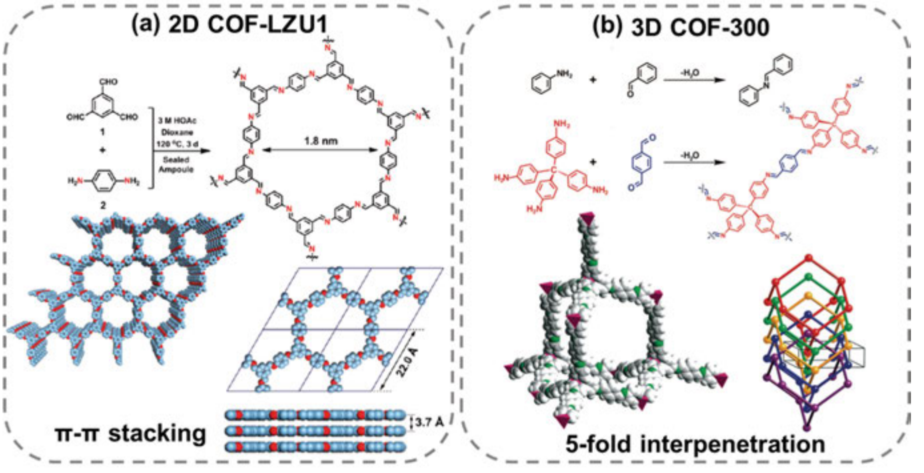

Figure 9 Schematic and structure of (a) 2D COF-LZU1.[59] Copyright (2011) , published by American Chemical Society. (b) 3D COF-300.[60] Copyright (2009), published by American Chemical Society.

Imine-linked COFs are synthesized via reversible Schiff-base condensation reactions between amines and aldehydes. According to the geometry of the building blocks, imine-linked COFs can be divided into either two-dimensional (2D) layered stacking structures or three-dimensional (3D) networks (Figure 9). Most imine-linked COFs with high crystallinity are prepared in toxic organic solvents using the solvothermal method which requires high reaction temperatures (>80 °C), a sealed vessel, long reaction times (>3 days).[59, 61] Additionally, an acid catalyst and water are necessary for the formation of crystalline imine-linked COFs. In the solvothermal method, organic building blocks are dissolved in an organic solvent to form a solution. Upon mixing the reactants, the polymerization reaction between the amine and aldehyde monomers starts immediately. The initial precipitates are typically amorphous. The sealed vessel has to be heated at a high temperature. Undergoing a long reaction time, the initial amorphous precipitates will transform into crystalline COFs in organic solvents.

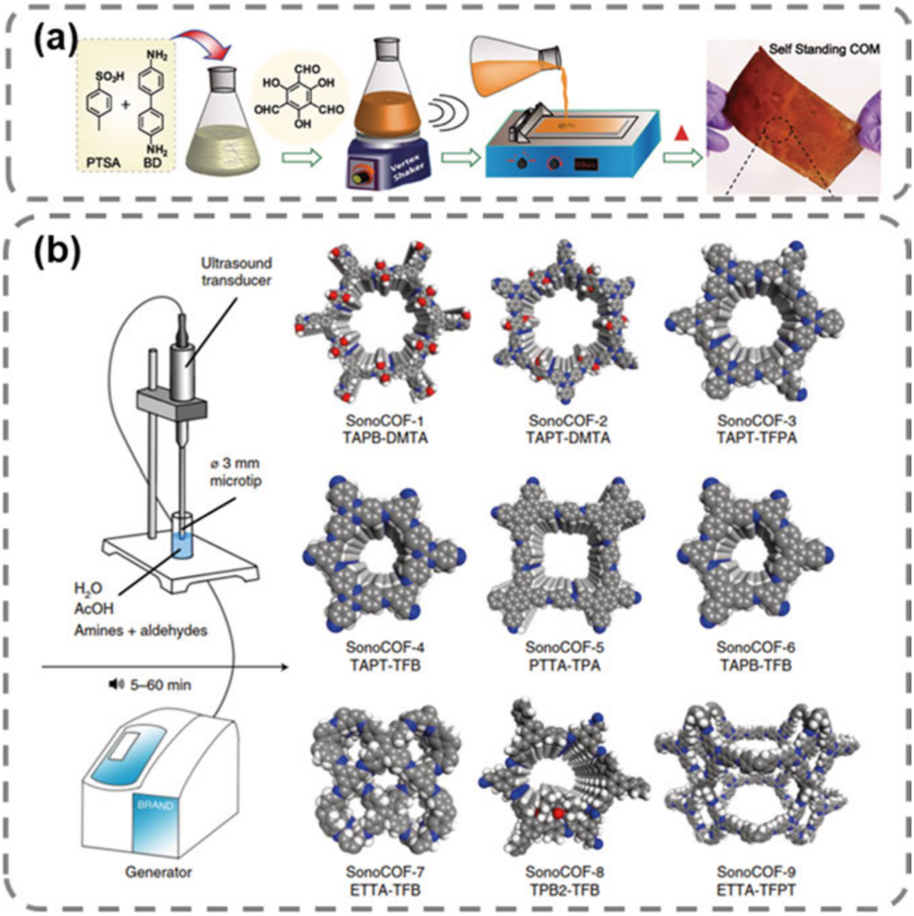

Figure 10 (a) Schematic representation of the COMs (M-TpBD) fabrication.[54] Copyright (2018) , published by Wiley. (b) Schematic of the sonochemical apparatus and reaction set-up, and the structures of the obtained COFs.[62] Copyright (2022), published by Springer Nature.

Although COFs prepared via the solvothermal method typically exhibit high crystallinity and have high surface areas, the use of toxic organic solvents incurs considerable economic and environmental costs. Furthermore, complex fabrication procedures significantly hinder their large-scale synthesis. Therefore, there has been much recent work exploring facile, scalable, and environmentally friendly methods of COF synthesis. Recently, Banerjee et al. fabricated a series of β-ketoenamine linked COFs with high crystallinity (Figure 10a) via a facile and scalable method.[54] Specifically, they baked the slurry of organic linkers with a p-toluenesulfonic acid (PTSA) catalyst and small amounts of water as the solvent. However, the use of large quantities of PTSA also incurs environmental costs. Cooper et al. have developed a sonochemical synthesis method to fabricate imine-linked COFs with high crystallinity and specific surface areas in aqueous solutions (Figure 10b).[62] This method involves sonicating the amine and aldehyde monomers in an aqueous acetic acid solution at ambient temperature for one hour. In this strategy, the application of high-energy ultrasound can promote organic monomers to dissolve and disperse in water, thereby enhancing their reactivity. Subsequently, the reaction between amine and aldehyde monomers is accelerated. Although these methods avoid the utilization of toxic organic solvents, which will greatly decrease the production cost of COFs and are better for environment, the requirement of high-energy ultra-sonicator perhaps limits the scale-up of the synthesis method. Therefore, developing a simple and mild strategy for the large-scale synthesis of imine-linked COFs in aqueous solution is imperative.

1.5 Cellulose

Cellulose, one of the most abundant renewable biopolymers on Earth, is found in the cell walls of plants and certain algae, as well as in the biofilms secreted by bacteria.[63-65] As a renewable and sustainable material, cellulose has been used by mankind for a long time, tracing back to handmade paper in the early Eastern Han Dynasty of ancient China. Cellulose consists of long chains of β-1,4-linked D-glucose units and possesses abundant hydroxyl (–OH) functional groups.[66] These groups enable the formation of robust hydrogen-bond networks within cellulose polymers, contributing to the high stability and high axial stiffness of cellulose polymers. Traditionally, cellulose has predominantly been utilized in the production of paper products. However, over the past decades, the emergence and advancement of nanocellulose, such as cellulose nanocrystals and cellulose nanofibers, have shown the immense potential of cellulose-based materials. These materials are now demonstrating significant potential for use in a diverse range of applications, including flexible electronics,[67] energy storage and conversion,[68] environmental and biotechnological applications.[69]

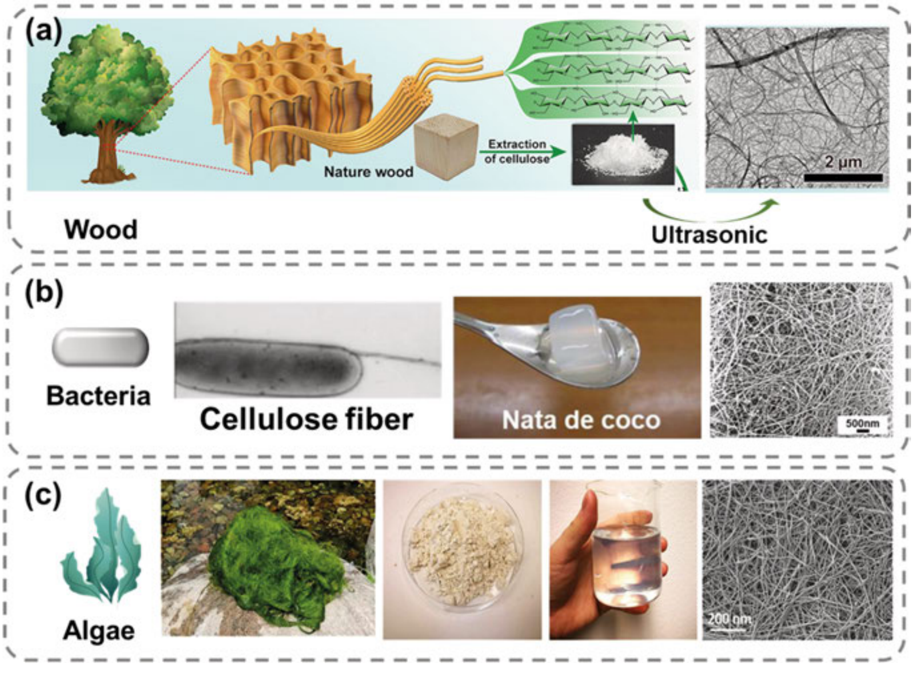

Figure 11 (a) Wood cellulose.[66] Copyright (2022), published by Frontiers. (b) Bacterial cellulose.[70] Copyright (2021), published by Springer Nature; (c) *Cladophora* cellulose (CC).[71] Copyright (2019) , published by American Chemical Society.

Table 1 Comparison of structural parameters of cellulose nanofibers obtained from wood,[72-75] bacteria,[64, 76-78] and *Cladophora* algae.[65, 78-79]

Cellulose nanofiber sources	**Crystallinity (%)**	**H_2O uptake ($m^2\ g^{-1}$)**	**Length (μm)**	**Diameter (nm)**	**Aspect ratio**	**Storage method**
Wood	~50-80	117-204	~0.1-0.5	~3−5	~20−30	aqueous solutions
Bacteria	~70-80	-	~0.6-1	~10−30	~20-100	hydrogels
Cladophora alga	> 95	52.8	~4-10	~15−30	~160-300	powders

Cellulose nanofibers typically have diameters between 3 and 50 nm, with lengths that can extend to several micrometers, giving a high aspect ratio. This form of cellulose exhibits excellent mechanical properties, and a large surface area, making them suitable for reinforcing materials in composites. Cellulose nanofibers obtained from wood, algae and bacteria can be formed into nanopapers which have been shown to be useful in applications such as biomedical devices[80-81] and electronics.[82-83] As shown in Table 1, cellulose nanofibers extracted from *Cladophora* algae have higher crystallinity, and larger lengths, diameters, and aspect ratios than those obtained from wood or bacteria. The high crystallinity of *Cladophora* cellulose nanofibers (CNFs) was confirmed by their lower H_2O uptake (Table 1),[79] since the adsorption of H_2O mainly occurs in the amorphous regions of cellulose nanofibers. Additionally, the high crystallinity of CNFs contributes to their outstanding mechanical strength and chemical stability making them particularly suitable for reinforcing composite materials.

Notably, CNFs can be preserved as a powder, unlike wood-based cellulose nanofibers which are stored in aqueous solutions and bacterial cellulose nanofibers which are stored as tangled hydrogels. This form of CNF powder disperses easily in water to form uniform hydrogels or suspensions due to its low hornification[65] —a feature that also allows dried CNF-based materials like aerogels or nanopapers to be redispersed in water as needed. This powder storage method significantly reduces shipping and storage costs, making it more suitable for commercial applications.

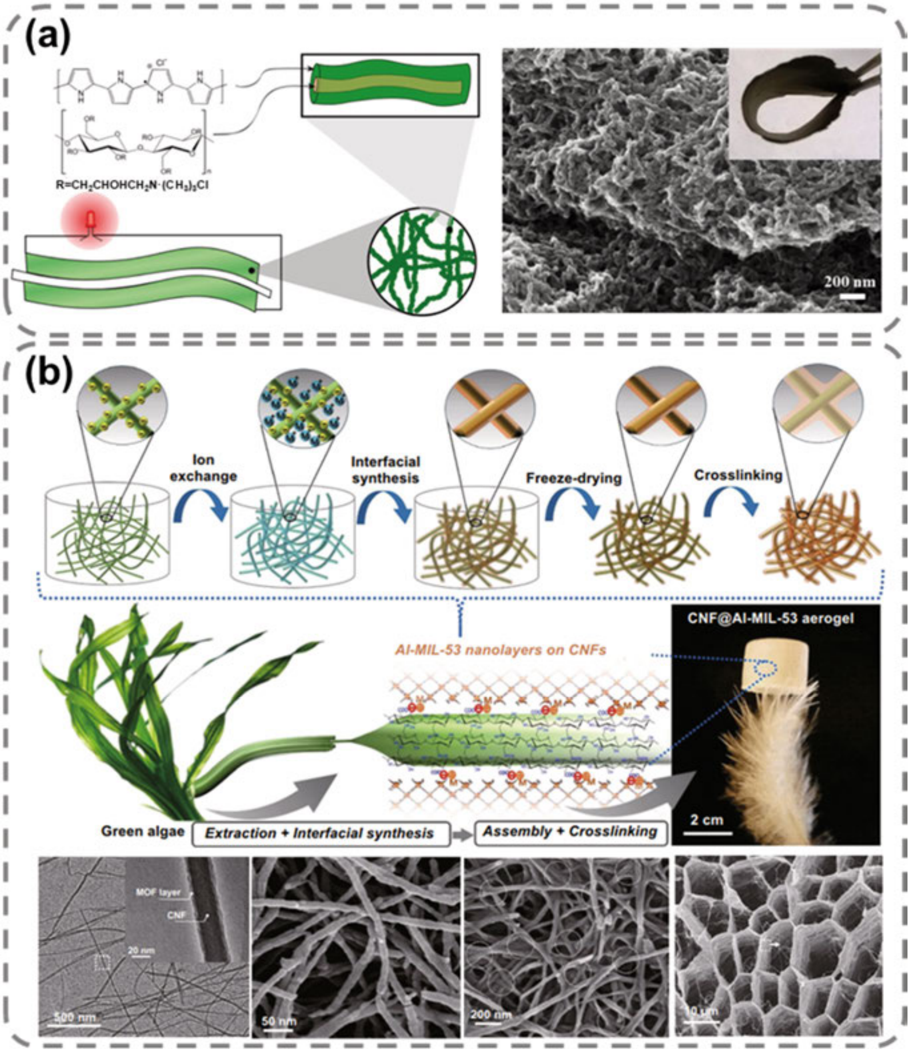

Figure 12 (a) Structure of PPy-nanocellulose fibers composites and its supercapacitor, and SEM images for PPy@c-NCFs,[84] Copyright (2015), published by American Chemical Society; (b) Schematic illustration and SEM images of the preparation of CNF@Al-MIL-53 (CAM) aerogels and TEM image of CNF@Al-MIL-53 nanofiber,[85] Copyright (2019), published by Springer Nature.

For instance, Wang et al. have reported the fabrication of polypyrrole (PPy)-nanocellulose fibers (NCFs) composites, in which NCFs were extracted from *Cladophora* algae.[84] The PPy@NCFs electrode exhibited high PPy mass loadings, reaching as much as 9 mg cm^{-2}. The PPy@NCFs supercapacitor (Figure 12a) demonstrated an electrode-normalized gravimetric capacitance of 127 F g^{-1} and a volumetric capacitance of 122 F cm^{-3} with a current density of 300 mA cm^{-2}. Zhou et al. reported CNF@MOF composites, processed into CNF@MOF aerogels (Figure 12b) with high mechanical strength but super elasticity (80% maximum recoverable strain, specific compression modulus 200 MPa $cm^3 g^{-1}$, specific stress 100 MPa $cm^3 g^{-1}$).[85] This exceptional mechanical performance can be attributed to the cross-linking of CNFs with continuous MOFs nanolayers, where CNFs were treated by TEMPO oxidation to form carboxylated CNFs. Furthermore, the lightweight aerogels obtained exhibit relatively a low thermal conductivity of ~ 40 mW $m^{-1} K^{-1}$ attributable to the cellular network structure and hierarchical porosity of the materials. Therefore, CNF is a promising substrate or template for the construction of freestanding and flexible composite materials.

2. Motivation and Aims

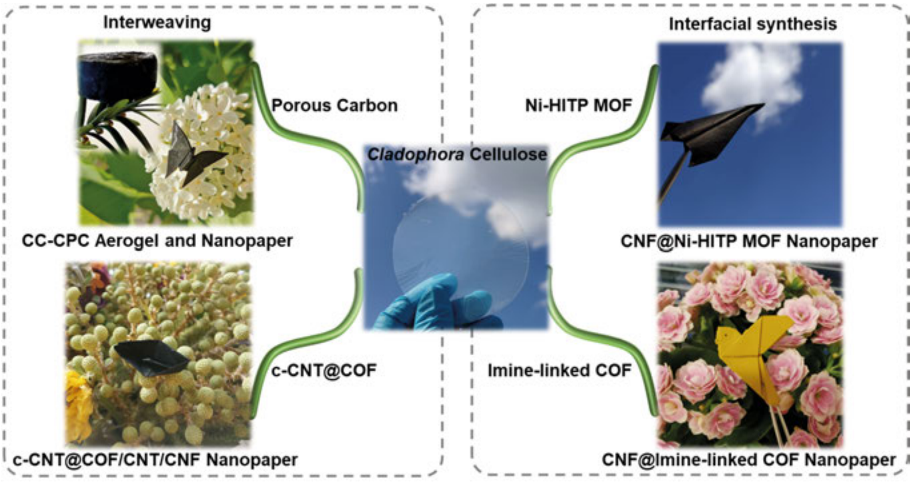

Figure 13 Photographs of CC-based aerogel and nanopaper composites.[86-88] These figures are adopted from **Paper I**, **III**, **and IV**. Copyright (2021), published by Elsevier Ltd under an open access CC-BY license. Copyright (2020), published by Elsevier Ltd under an open access CC-BY license. Copyright (2023), published by American Chemical Society under an open access CC-BY 4.0 license.

Porous materials, including PCs, MOFs, and COFs, demonstrate significant potential in various application fields due to their abundant microporous and mesoporous structures, as well as their high surface areas. Nevertheless, these materials face several challenges, notably their environmentally unfriendly fabrication methods and their poor processability. Specifically, the fabrication of PC typically involves a carbonization/activation process. These activation process, especially chemical activation, require the use of corrosive agents, which are harmful to our environment and increase production costs. Additionally, the synthesis of COFs usually involves the utilization of toxic organic solvents, which also generate environmental and production costs. The poor processability of porous materials as powder primarily arises from their insolubility and infusibility, which limits shaping these materials into diverse forms. This limitation significantly impedes their broader applications.

Therefore, we decided to develop new strategies to synthesize porous materials through environmentally friendly methods. Specifically, we utilized a naturally abundant biopolymer, CC, to prepare PCs without using any corrosive agents. Additionally, a series of imine-linked COFs were prepared in an aqueous solution, avoiding the use of toxic organic solvents.

To overcome their poor processability, we introduced a flexible substrate, CNF, to integrate with porous materials and form freestanding nanopapers and aerogels (Figure 13). In this thesis, we employed two strategies to integrate porous materials and CNF. Firstly, we used CNF as a flexible substrate, interweaving it with porous materials (including PC and COF-based materials) in aqueous solutions to create freestanding and flexible cellulose-based composites. Secondly, we used carboxylated CNF as a template, using interfacial chemistry to synthesize MOFs or COFs on the carboxylated CNF surface in aqueous solutions. Ultimately, we prepared a series of cellulose-based composite nanopapers, which possess excellent mechanical properties and can be folded into various shapes (Figure 13).

Additionally, based on the properties of the porous materials contained in the freestanding composites, they can be used for a variety of applications, including as flexible energy storage devices, solar vapor generators and adsorption of CO_2 and organic pollutant.

3. Fabrication and Characterization of Porous Materials

3.1 Porous Carbon Derived from *Cladophora* cellulose

3.1.1 Synthesis

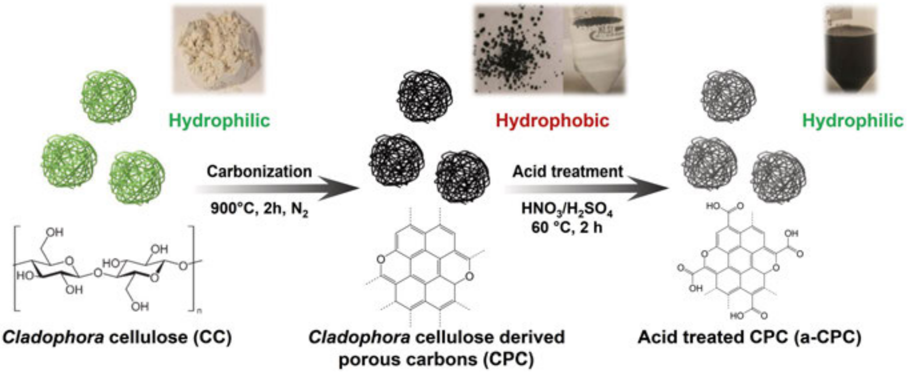

Figure 14 Schematic illustration of the preparation of *Cladophora* cellulose-derived porous carbon (CPC) and acid-treated CPC (a-CPC) from *Cladophora* cellulose (CC).[87] The figure is adopted from **Paper I**. Copyright (2021), published by Elsevier Ltd under an open access CC-BY license.

Most PCs are prepared through the carbonization and activation of carbon precursors. Cellulose is a promising bio-precursor because it is carbon-rich and abundant biopolymer on Earth, which can be extracted from various sources such as wood, bamboo, and algae. Typically, preparing PC from cellulose precursors requires carbonization, activation by a corrosive agent, and purification. This complex procedure increases the production cost and the use of corrosive agents is harmful to the environment. Additionally, the obtained PC powders are always hydrophobic and insoluble, making them difficult to process and limiting their practical applications.

In **Paper I**, a one-step physical carbonization/activation method to prepare PC derived from CC was introduced. The pyrolysis product was named CC-derived PC (CPC) (Figure 14). Since the hydrophilic OH groups were removed during pyrolysis, the obtained CPC became hydrophobic and was difficult to disperse in water, thereby resulting in the poor processability in water (Figure 14). To address the hydrophobicity, the obtained CPC was post-modified with an acid treatment method to introduce COOH groups, increasing their hydrophilicity. The acid-treated CPC (a-CPC) was easily dispersed in water, indicating significant hydrophilicity and water dispersibility (Figure 14).

3.1.2 Structure and Properties

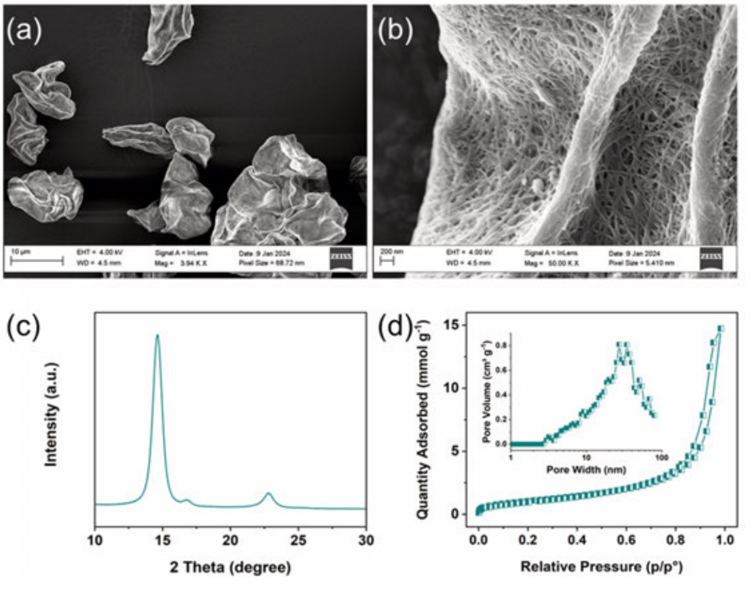

Figure 15 (a-b) SEM images, (c) XRD pattern, and (d) N_2 adsorption and desorption isotherms of CC powder.[87] Figure 15d is adopted from **Paper I**. Copyright (2021), published by Elsevier Ltd under an open access CC-BY license.

From the SEM images, the CC particles formed micro-flowers with a few microns in diameter, composed of CC nanofiber with a diameter of ≈ 20−30 nm (Figures 15a-15b). These CC nanofibers showed intertwined structures, resulting in the formation of mesopores around 30 nm in diameter (Figure 15d). The specific surface area of CC can reach 85 $m^2\ g^{-1}$. The XRD pattern displays the characteristic peaks of CC at 2 θ ≈ 13.1, 15.2, 20.2°, corresponding to the (100), (010), and (110) reflections of CC (Figure 15c), respectively.

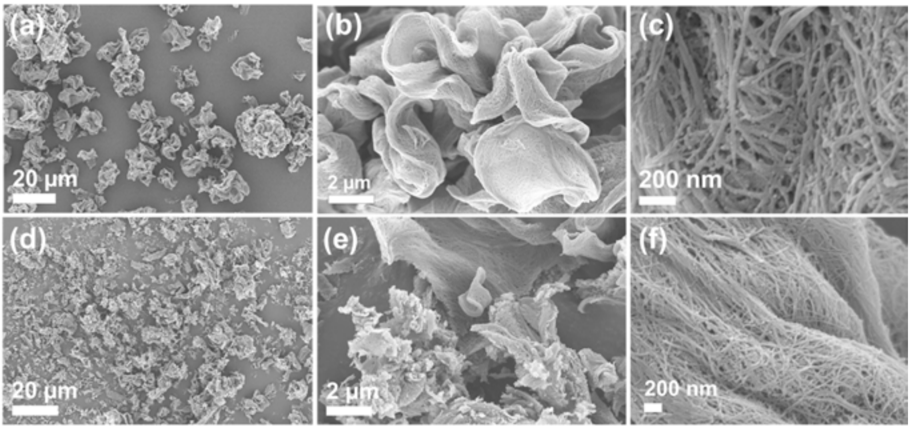

Figure 16 SEM images of (a-c) CPC and (d-f) a-CPC.[87] These figures are adopted from **Paper I**. Copyright (2021), published by Elsevier Ltd under an open access CC-BY license.

CC and CPC particles have similar sizes and morphologies which demonstrates the stability of the CC nanostructure (Figure 16a-16c). This result is attributed to the high crystallinity of CC (Figure 15c). The specific surface area of CPC was measured as being 507.2 $m^2\ g^{-1}$, which is higher than that of CC. The obtained CPC has rich micropores centered at 0.7 and 1.2 nm (Figure 17b). The formation of micropores in CPC can be attributed to that the generation of gaseous products (water vapor, and CO_2 molecules) during the pyrolysis of CC act as activation agents and templates, generating porous structures.

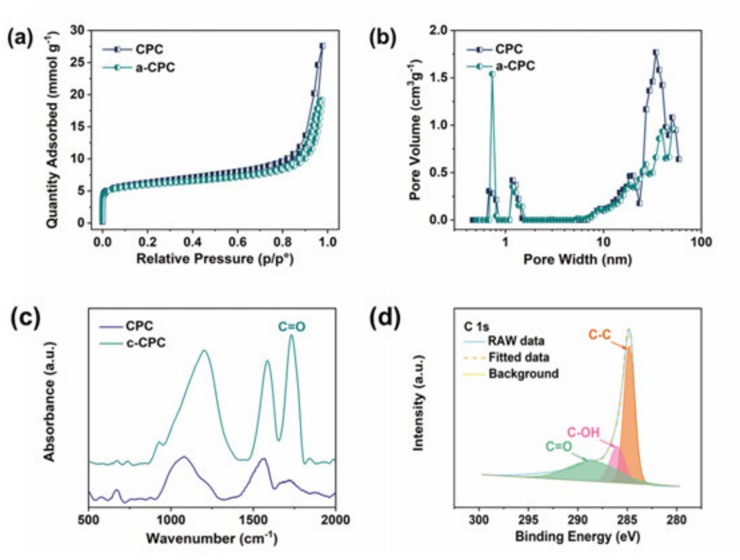

Figure 17 (a) N_2 adsorption and desorption isotherms of CPC and a-CPC measured at 77K; (b) pore size distributions of CPC and a-CPC; (c) IR spectra of CPC and a-CPC; (d) high-resolution C1s XPS spectrum of a-CPC.[87] These figures are adopted from **Paper I**. Copyright (2021), published by Elsevier Ltd under an open access CC-BY license.

The morphology of a-CPC differs from that of CPC, indicating that the micro-flower-shaped CPC particles were broken into smaller pieces after acid treatment (Figures 16d-16f). While, the nanofiber structure was retained in a-CPC after acidification. The specific surface area of CPC was measured as being 496.2 $m^2\ g^{-1}$ (Figure 17a), showing a slight decrease compared to CPC. As shown in Figure 17b, the micropores of CPC are therefore retained when converting to a-CPC and the formation of mesoporous structures can be attributed to the intertwined nanofibers structures.

From the Infrared (IR) spectra of CPC and a-CPC (Figure 17c), we can observe a peak at 1700 cm^{-1} in a-CPC, attributed to C=O stretching vibration, which is absent in CPC. Additionally, the strong shoulder peak at 288.7 eV can be observed in the X-ray photoelectron spectroscopy (XPS) spectrum of a-CPC, attributed to the carbons of the C=O and O–C=O groups (Figure 17d). Both of these results indicate that carboxylic groups have been successfully introduced into a-CPC.

3.2 Redox-Active COF

As previously stated, COFs are a new family of crystalline porous organic polymers, assembled by covalent bonds between organic building blocks. They possess high surface areas, long-range ordered porous structures, and tuneable pore size and structures, making COFs highly promising for electrochemical energy storage applications.[89] Specifically, the high surface area of COFs enhances adsorption of electrolyte ions on their electrode surfaces, thereby optimizing double-layer capacitances. Additionally, their ordered porous structures facilitate rapid transport of electrolyte ions through the materials, thereby enhancing the rate capability of the electrodes. The diversity of organic building blocks allows the integration of redox-active moieties within the frameworks, thereby achieving high theoretical capacities and energy densities. However, most COFs exhibit low electrical conductivity, which hinders charge transfer within the frameworks and thus limits their electrochemical performances.

Paper III introduces an interfacial synthesis method to prepare carboxylated multi-walled carbon nanotubes (c-CNTs) and redox-active COF composites (c-CNT@COF). The thickness of the redox-active COF layer on the surface of the c-CNTs can be controlled by adjusting the mass ratio between the c-CNT and the redox-active COF. In this system, the c-CNT acts as a conductive skeleton, facilitating electron transfer in the redox-active COF. After adjusting the mass ratio, c-CNT@COF structure with only a few COF layers can be obtained, which provides a short pathway for the diffusion of electrolyte through the COF layers. This combination of a conductive skeleton for electron transfer, and a short pathway for electrolyte diffusion, enable the charge/discharge process to achieve a high rate, even at a high current density. Consequently, the redox-active sites within the COF layer can be efficiently utilized during electrochemical processes.

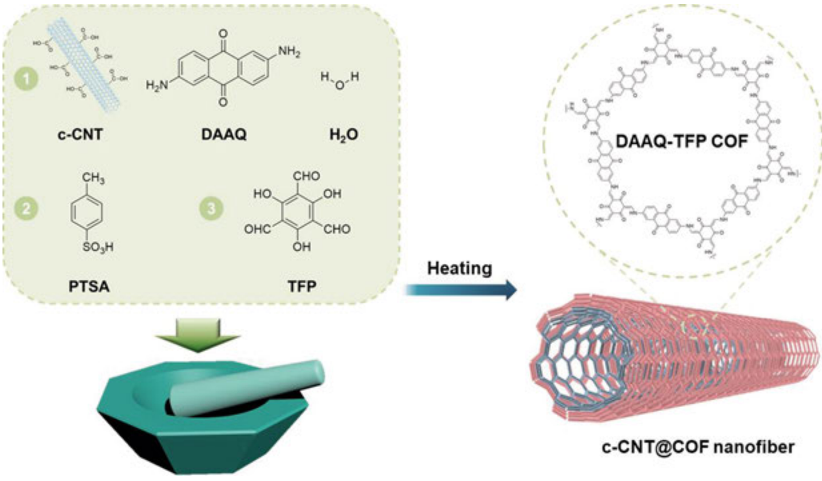

Figure 18 Schematic of the synthesis of c-CNT@COF.[88] The figure is adopted from **Paper III**. Copyright (2020), published by Elsevier Ltd under an open access CC-BY license.

3.2.1 Synthesis

Figure 18 shows the preparation of c-CNT@COF composites through an interfacial synthesis method. The first step involves mixing c-CNT, DAAQ (2,6-diaminoanthraquinone), and water. The second involves mixing PTSA with the slurry obtained in step 1. The third step involves mixing TFP (1,3,5-triformylphloroglucinol) with this mixture to form the final slurry, which is subsequently heated at 60°C, 90°C, and 120°C for one day at each temperature, respectively. By adjusting the mass ratio between c-CNT and COF, we obtained three products with controlled compositions, named c-CNT@COF-1, -2, and -3. The COF contents of CNT@COF-1, -2, and -3 were determined to be 76.6 wt%, 48.6 wt%, and 41.7 wt%, respectively, calculated from thermogravimetric (TGA) curves (Figure 19).

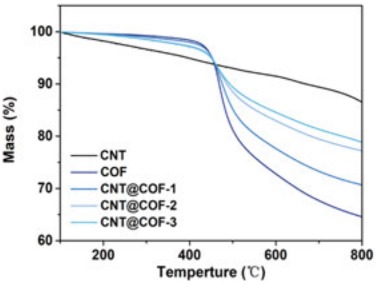

Figure 19 TGA curves of c-CNT, the pure COF and the three c-CNT@COFs composites under a N_2 atmosphere.[88] The figure is adopted from **Paper III**. Copyright (2020), published by Elsevier Ltd under an open access CC-BY license.

3.2.2 Structure and Properties

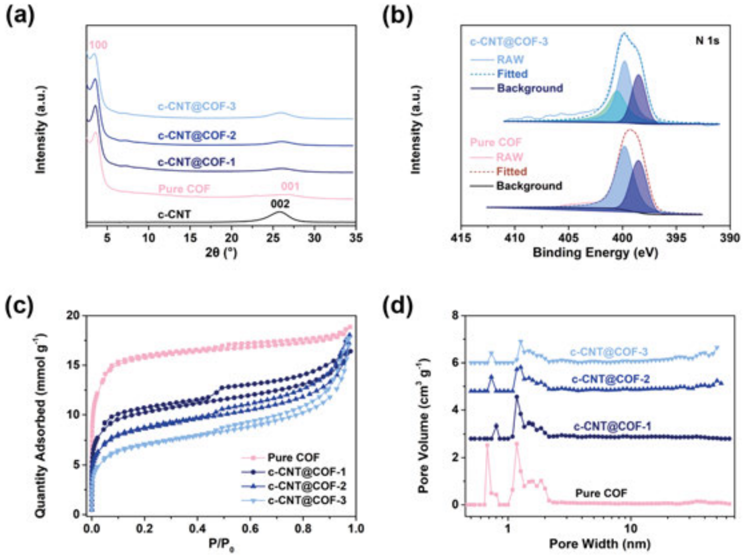

Figure 20 (a) Powder X-ray diffraction patterns of the pure c-COF and CNT@COF composites; (b) high-resolution N1s XPS spectrum of the pure COF and c-CNT@COF-3 and the deconvoluted results; (c) N_2 adsorption and desorption isotherms recorded at 77 K; (d) pore size distributions of the pure COF and c-CNT@COFs calculated from the adsorption isotherms.[88] These figures are adopted from **Paper III**. Copyright (2020), published by Elsevier Ltd under an open access CC-BY license.

From the XRD patterns (Figure 20a), all samples exhibit a characteristic peak at 2θ ≈ 3.6°, corresponding to the 100 reflection plane of DAAQ-TFP COF, which evidence the formation of COFs in the obtained composites. Additionally, we selected c-CNT@COF-3, which had the thinnest COF layer of all the composites tested (c-CNT@COF-1, 2, 3) for XPS analysis (Figure 20b). Specifically, we can observe a shift in the N1s binding energy of c-CNT@COF-3 towards to a higher energy than that of pure COF. In the c-CNT@COF-3 sample, three peaks were identified through deconvolution, including one at 400.5 eV (Figure 20b). This particular peak, which is not present in pure COF, results from N atoms in amide linkages (−C(=O)N−) at the interface between c-CNTs and COF. These amide linkages are created by the reaction of carboxylic acid groups on c-CNTs with amine groups on DAAQ. These results indicate a change in the bonding mode of N atoms within the c-CNT@COF-3 composites.

As the COF content decreased, the BET surface area of samples decreased from 1288.3 $m^2 g^{-1}$ (for the pure COF) to 834.3, 709.8 and 576.7 $m^2 g^{-1}$ for c-CNT@COF-1, 2, and 3, respectively. The microporous volume of the c-

CNT@COF composites decreased significantly as the COF content was reduced (Figure 20c and 20d). Additionally, the mesoporous structure of c-CNT@COFs were formed by the intertwining of c-CNT@COF nanofibers (Figures 20d and 21). In pure COF, the mesoporous structure is attributed to the stacking of the COF flakes. Both c-CNT@COF nanofibers and pure COF flakes can be observed by SEM (Figure 21).

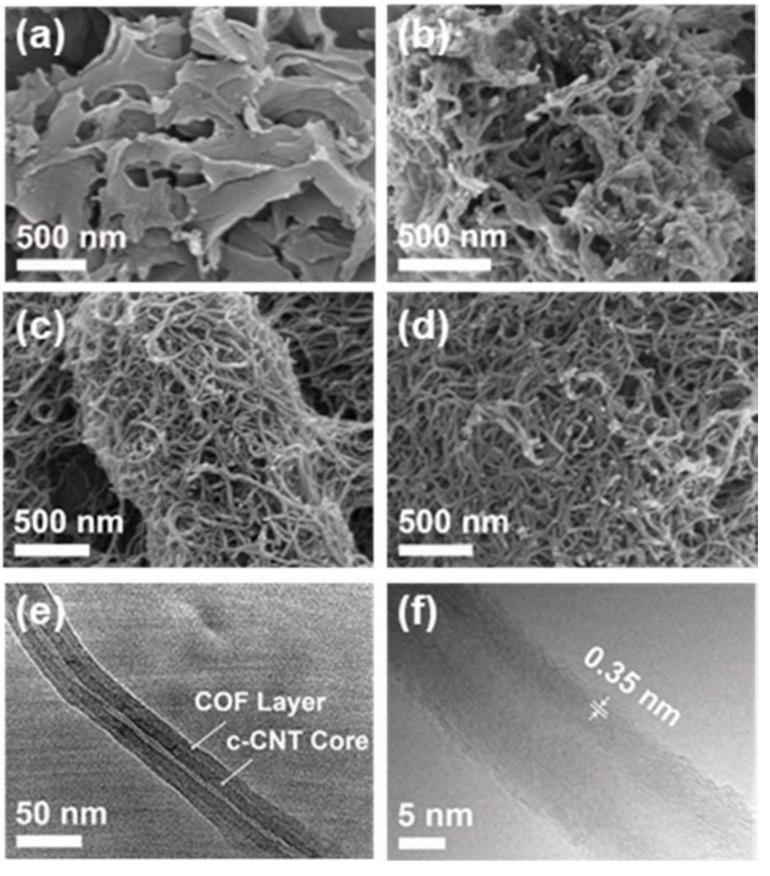

Figure 21 SEM images of (a) pure COF, (b) c-CNT@COF-1, (c) c-CNT@COF-1, and (d) c-CNT@COF-3; (e-f) transmission electron microscopy (TEM) images of c-CNT@COF-3.[88] These figures are adopted from **Paper III**. Copyright (2020), published by Elsevier Ltd under an open access CC-BY license.

As the COF content decreased, the c-CNT@COF-3 composites show a typical nanofiber structure, indicating COF layers are completely coated on the surface of c-CNTs (Figures 21d-21f). The lowest content of COF results in the thinnest COF coating, demonstrating that the thickness of the COF nanolayer on the surface of c-CNTs can be precisely controlled. As shown in Figure 21e, the c-CNT@COF-3 nanofiber shows a typical tube-type core-shell structure and the COF nanolayer has a thickness of approximately 10 nm. From TEM image (Figure 21f), we observe the stacking of COF layers with an interlayer spacing approximately 0.35 nm, which corresponds to the d-spacing of the 001 planes of COFs.

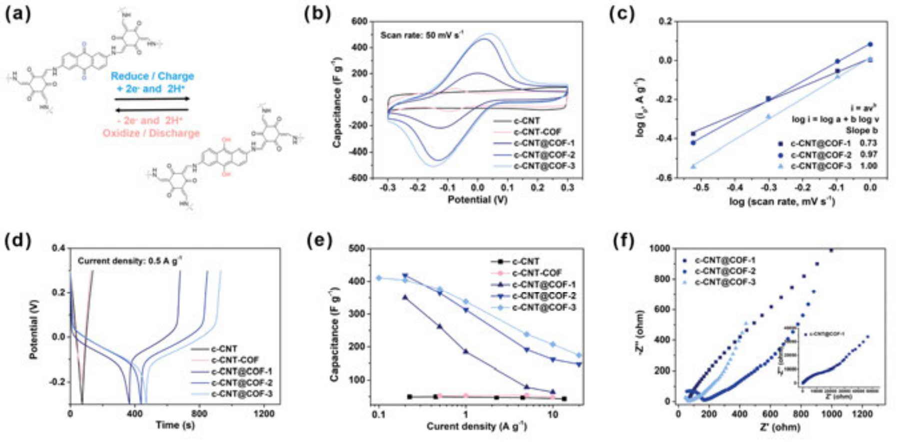

Figure 22 (a) The reversible quinone to hydroquinone transformation in DAAQ-TFP COF showing its redox (charge/discharge) mechanism; (b) comparison of cyclic voltammetry curves of the c-CNT, c-CNT@COFs and c-CNT-COF electrodes at a same scan rate of 50 mV s^{-1} and a voltage range of –0.3 to +0.3 V vs. Ag/AgCl; (c) plots of log (i_p) versus log (n) for c-CNT@COFs electrodes, where i_p is the peak current and n is the scan rate; (d) comparison of galvanostatic charge-discharge (GCD) curves and (e) gravimetric capacitances of the c-CNT, c-CNT-COF and c-CNT@COFs electrodes. The capacitances were calculated from the GCD curves; (f) electrochemical impedance spectra of the c-CNT@COFs electrodes.[88] These figures are adopted from **Paper III**.

c-CNT@COFs have significant potential for electrochemical energy storage, because they have conductive cores, porous structures, accessible redox-active units and tuneable nanofibrous structures. Electrochemical measurements of c-CNT@COFs was conducted using a traditional three-electrode system, assembled with an Ag/AgCl reference electrode, a Pt foil counter electrode, and a working electrode composed of 80 wt% c-CNT@COFs, 10 wt% CNT and 10 wt% PVDF, in a 0.5 M H_2SO_4 aqueous electrolyte. Additionally, a c-CNT-COF electrode was prepared by mixing pure COF with c-CNT, in which the COF content was equal to that of the c-CNT@COF-3. The c-CNT@COF-3 electrode demonstrated the highest current responses of all the materials tested (Figure 22b), after normalizing into gravimetric capacitances (using the total mass of the working electrodes, more information provided in **Paper III**). Notably, the CV curve of the c-CNT-COF electrode had very small redox peaks, and its capacitance was significantly lower than that of the c-CNT@COF-3 electrode. These smaller peaks suggest that most of the redox-active sites in the COF did not react and contribute to the capacitance. The limited utilization of redox-active sites in the c-CNT-COF electrode can be attributed to sluggish electron transfer and concomitant slow ion diffusion, arising from limited contact between the COF flakes and c-CNT. In contrast, the high current responses of c-CNT@COF-3 can be attributed to its enhanced conductivity and greater access to redox-active sites due to it having the highest c-CNT content and the thinnest COF nanolayer. The c-CNT@COF-3 electrode has compact nanofibrous structures with a large interfacial area, which allows for efficient electron transfer and exposes more redox-active sites, effectively shortening the ion transport path. The relationship between the CV peak current (i_p) and the scan rate (v), according to the formula: $i_p = av^b$, can be used to study the kinetics of the redox reactions (Figure 22c). The b value of close to 1.00 is obtained with the c-CNT@COF-3, further illustrating that redox reactions take place on or near the surface of the COF nanolayers. The reaction occurred without diffusion-limited mass transport, thereby facilitating rapid charge/discharge cycles and efficient utilization of redox-active sites. Remarkably, c-CNT@COF-3 exhibited high capacitances of 403.6 F g^{-1} at 0.2 A g^{-1} and 376.2 F g^{-1} at 0.5 A g^{-1}, significantly higher than the other electrodes tested (Figure 22d-22e). After deducting the capacitance contribution of the CNT, the capacitance of the COF in the c-CNT@COF-3 composite electrode was calculated as 930.6 F g^{-1} at 0.5 A g^{-1} (more information provided in **Paper III**). This is in good agreement with the theoretical capacitance of the COF which was calculated as 938.8 F g^{-1}. Hence, 99.1% of the redox-active sites of COF were utilized in the c-CNT@COF-3 electrode, which was higher than c-CNT@COF-1 (38.4 %), c-CNT@COF-2 (83.0 %), and c-CNT-COF (6.3 %). Electrochemical impedance spectroscopy results confirmed that c-CNT@COF-3 has lower charge transfer resistances and higher onset frequencies, indicating efficient electron transfer, enhanced charge storage site accessibility, and rapid ion transport (Figure 22f, more information provided in **Paper III**). These features evidence that c-CNT@COF-3 electrode exhibits high capacitance and efficient utilization of the redox active sites.

3.3 Imine-Linked COFs

COFs, assembled through covalent bonding between organic monomers, are crystalline polymers characterized by permanent porosity. These structures provide significant promise for a range of applications including catalysis,[3] storage and separation,[51] energy storage and conversion.[58] To achieve highly crystalline COFs, the solvothermal method is often used to the targeted synthesis. However, this method usually involves the use of toxic organic solvents, high temperatures, elevated pressure, and requires an inert atmosphere or vacuum. These harsh experiment conditions lead to high production costs that hinder large-scale preparation of COFs.

Recently, various methods have been developed to synthesize imine-linked COFs in aqueous solutions. For instance, Copper et al. utilized a sonochemical method to create imine-linked COFs,[90] while Zhang et al. synthesized COF-LZU 1 in water containing dissolved CO_2 at high pressure (4.5 MPa).[91] By avoiding the use of organic solvents, these approaches not only reduce the costs associated with producing imine-linked COFs, but also enhance their environmental sustainability. Despite these advancements, challenges remain in scaling up the production of imine-linked COFs using sonochemical and high-pressure methods. Here, **Paper IV** introduces a simple and environmentally friendly method to fabricate a series of imine-linked COFs.

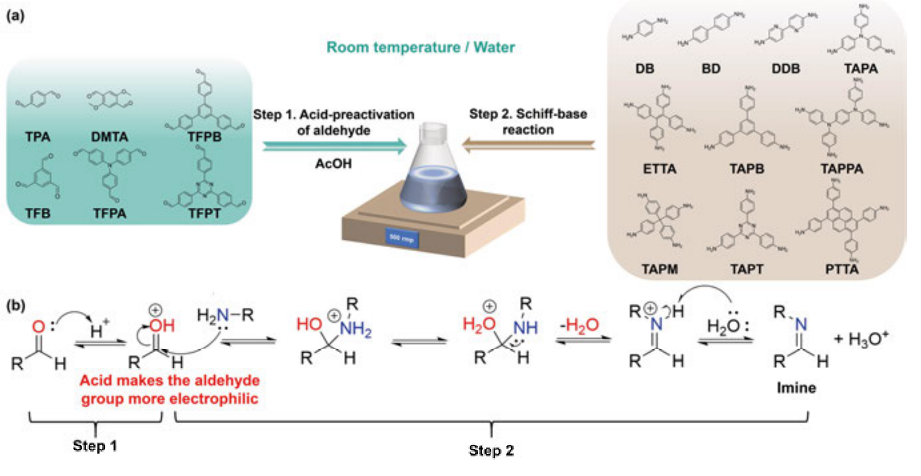

Figure 23 (a) Schematic synthesis of imine-linked COFs in aqueous solution; (b) formation process of imine through nucleophilic addition of amine on acid-preactivated aldehyde.[86] These figures are adopted from **Paper IV**. Copyright (2023), published by American Chemical Society under an open access CC-BY 4.0 license.

3.3.1 Synthesis

As shown in Figure 23, we synthesized a series of imine-linked COFs in aqueous solution under ambient conditions. The process began by stirring aldehyde monomers in an aqueous solution of acetic acid for 30 minutes. This step is critical, as the acetic acid interacts with the aldehyde monomers, enhancing the dispersion of the aldehyde within the aqueous solution and increasing its electrophilicity of the aldehyde, thereby facilitating a more efficient reaction with the amine group. Subsequently, we introduced an aqueous solution of amine monomers to the mixture under continuous stirring, which facilitated the subsequent Schiff-base reaction. The synthesis method was named as aldehyde preactivation method (AP method).

3.3.2 Structure and Properties

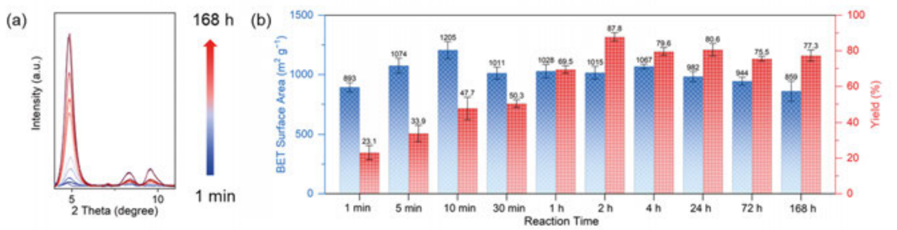

Figure 24 (a) X-ray diffraction patterns of the crude TFB-DB COF samples collected at different reaction intervals (from 1 min to 168 h). (b) Comparison of the yield and BET surface area of purified TFB-DB COFs after different reaction times. All of the crude products were washed with water to remove residual acetic acid and unreacted DB monomer prior to the measurements. The purified samples were washed with both water and acetone to remove any acetic acid and unreacted monomers prior to the measurements.[86] These figures are adopted from **Paper IV**. Copyright (2023), published by American Chemical Society under an open access CC-BY 4.0 license.

To evaluate the AP method, we synthesized a series of TFB-DB COFs, across different reaction times, where TFB stands for 1,3,5-triformylbenzene and DB represents 1,4-diaminobenzene. We obtained crystalline TFB-DB COF within a very short reaction time (1 minute) (Figure 24a). The yield of the collected crystalline TFB-DB COF was 23.1%, and the BET surface area is up to 893 m^2 g^{-1} (Figure 24b). When the reaction time was extended to 2 hours, the COF yield reached its maximum value of 87.8% (Figure 24b). Over extended the reaction times, 4–168 hours, the yield remained between 80.6% and 75.5%. These results are consistent with time-dependent XRD analysis (Figure 24a), indicating that most monomers polymerize within the initial two hours. Notably, extending the reaction time (4–168 hours) slightly reduces the surface area and yield of product. This phenomenon may be attributed to the reversibility of imine bonds, where an abundance of water in the reaction leads to the hydrolysis of the formed imines.

The formation of crystalline imine-linked COFs in aqueous solutions occurs at the onset of the reaction (Figure 24a). This crystallization process in aqueous solution differs from traditional solvothermal method, where amorphous precipitates initially form in organic solvents. In the solvothermal method, the reaction in organic solvents requires reaction times of several days at high temperatures to enable the initial amorphous precipitates to transform into crystalline COFs. We hypothesize that the crystallization mechanism of imine-linked COFs relies on dynamic imine exchange, where imine bonds break and reform at an appropriate rate, leading to self-correcting defects and crystallization of COFs.

In traditional solvothermal method, aldehyde and amine monomers are dissolved in an organic solvent. Consequently, the formation rate of imine bonds is rapid upon the addition of acetic acid to the mixed aldehyde and amine solutions, resulting in initial amorphous precipitates. To achieve crystalline COFs, it is necessary to prolong the reaction at high temperatures, ensuring the imine bond exchange, allowing self-correction of the defects and subsequent crystallization. In our AP method, the acid pre-activated aldehyde monomers formed a suspension and exhibit increased reactivity, but most remain undissolved, which limits the reaction rate with amine monomers. Consequently, the formation rate of imine bonds in aqueous solution is lower than that of organic solvents. The breaking rate of imine bonds in aqueous solution is higher than that of organic solvents due to the presence of larger amounts of water, which can drive back the Schiff-base reaction. Therefore, the imine bonds break and reform in the AP method may proceed at an appropriate rate at the onset of reaction. As a result, we are able to obtain crystalline TFB-DB COF in a short reaction time.

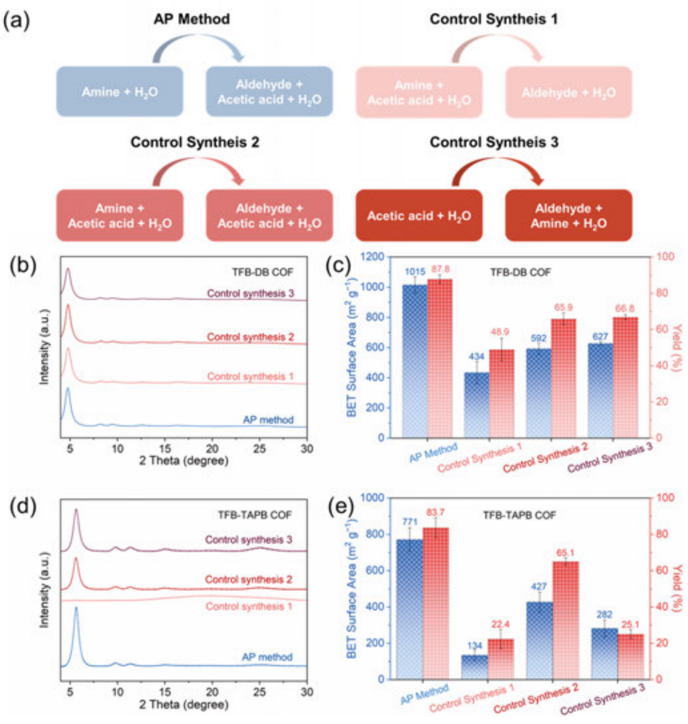

Figure 25 (a) Illustration of AP method and control synthesis 1−3; comparison of the COFs synthesized by the AP method and the control conditions 1−3, all after 2 h of reacting: (b) XRD patterns of the purified TFB-DB COF; (c) the yield and BET surface area of TFB-DB COF (d) XRD of the purified TFB-TAPB COF; and (e) yield and BET surface area of the TFB-TAPB COF. The purified samples were washed with both water and acetone to remove any acetic acid and unreacted monomers prior to the measurements.[86] Figure 25b-25e are adopted from **Paper IV**. Copyright (2023), Published by American Chemical Society under an open access CC-BY 4.0 license.

We designed different control experiments, as described in Figure 25a, to study the structure of imine-linked COFs synthesized under different orders of acid addition. As shown in Figures 25b-25e, two imine-linked COFs, TFB-DB COF and TFB-TAPB COF, were synthesized via the AP-method and the control methods 1-3, in which all reaction occurred over 2 hours. The imine-linked COFs synthesized via the AP method possessed higher crystallinity, yield, and BET surface area than those synthesized using control methods 1-3 (Figures 25c and 25e). Notably, TFB-TAPB COF synthesized via control method 1 had very low crystallinity, indicating the collected products were predominantly amorphous (Figure 25d), resulting in a low BET surface area. Meanwhile, the yield of the collected product was only 22.4%, indicating that most amine monomers had not yet reacted with aldehyde monomers. These results indicate that the amine monomers, protonated by acetic acid, lose their reactivity with the aldehyde monomers, thereby hindering the formation of TFB-TAPB COF and resulting in a low yield.

According to these results, we can infer that pre-activating the aldehyde monomers in aqueous solution is a crucial step in the formation of imine-linked COFs with excellent crystallinity, large surface area, and high yield.

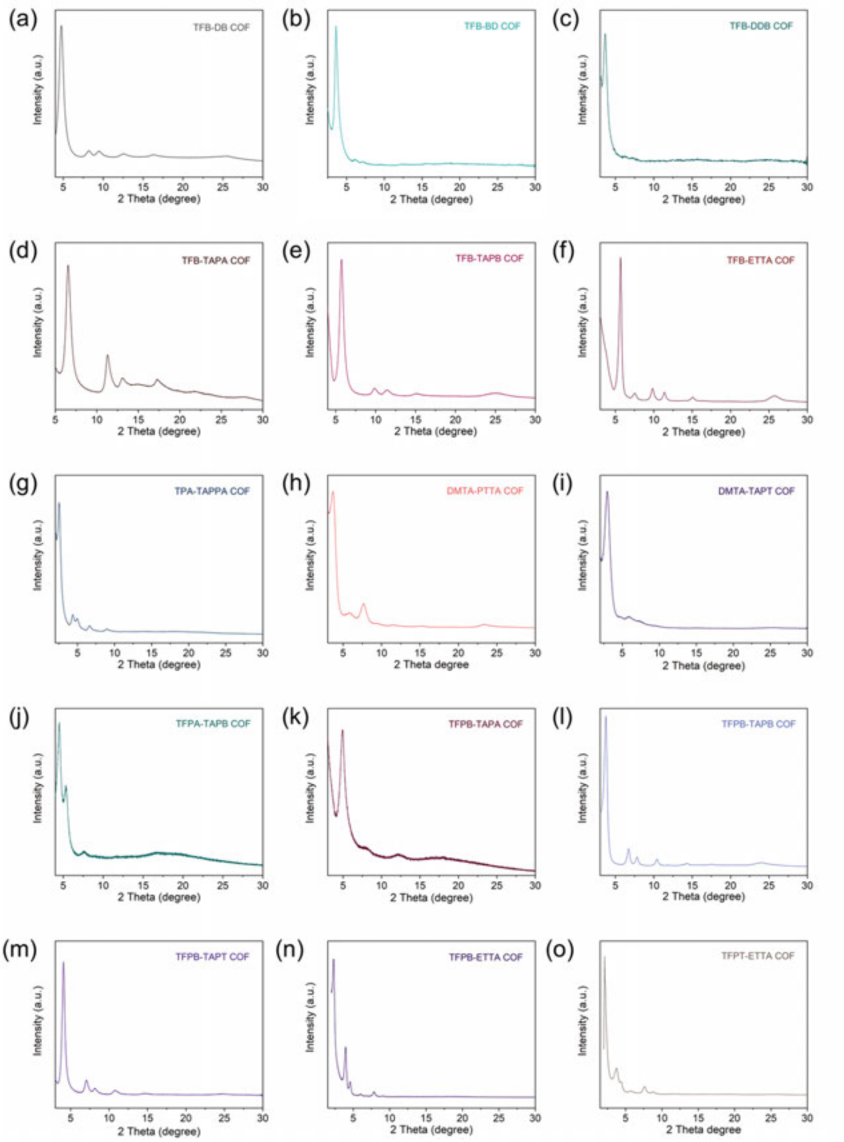

Figure 26 XRD patterns of TDB-DB COF (a), TFB-BD COF (b), TFB-DDB COF (c), TFB-TAPA COF (d), TFB-TAPB COF (e), TFB-ETTA COF (f), TPA-TAPPA COF (g), DMTA-TAPT COF (h), DMTA-PTTA COF (i), TFPA-TAPB COF (j), TFPB-TAPA COF (k), TFPB-TAPB COF (l), TFPB-TAPT COF (m), TFPB-ETTA COF (n) and TFPT-ETTA COF (o).[86] These figures are adopted from **Paper IV**. Copyright (2023), published by American Chemical Society under an open access CC-BY 4.0 license.

To demonstrate the broad applicability of the AP method, we conducted a series of reactions utilizing various amine and aldehyde monomers to fabricate additional imine-linked COFs. In **Paper IV**, we introduced 15 different imine-linked COFs with high crystallinity (Figure 26) and high BET surface area (459−2487 m^2 g^{-1}, Figure 27): TFB-DB COF, TFB-BD COF, TFB-DDB COF, TFB-TAPA COF, TFB-TAPB COF, TFB-ETTA COF, TPA-TAPPA COF, DMTA-PTTA COF, DMTA-TAPT COF, TFPA-TAPB COF, TFPB-TAPA COF, TFPB-TAPB COF, TFPB-TAPT COF, TFPB-ETTA COF, and TFPT-ETTA COF.

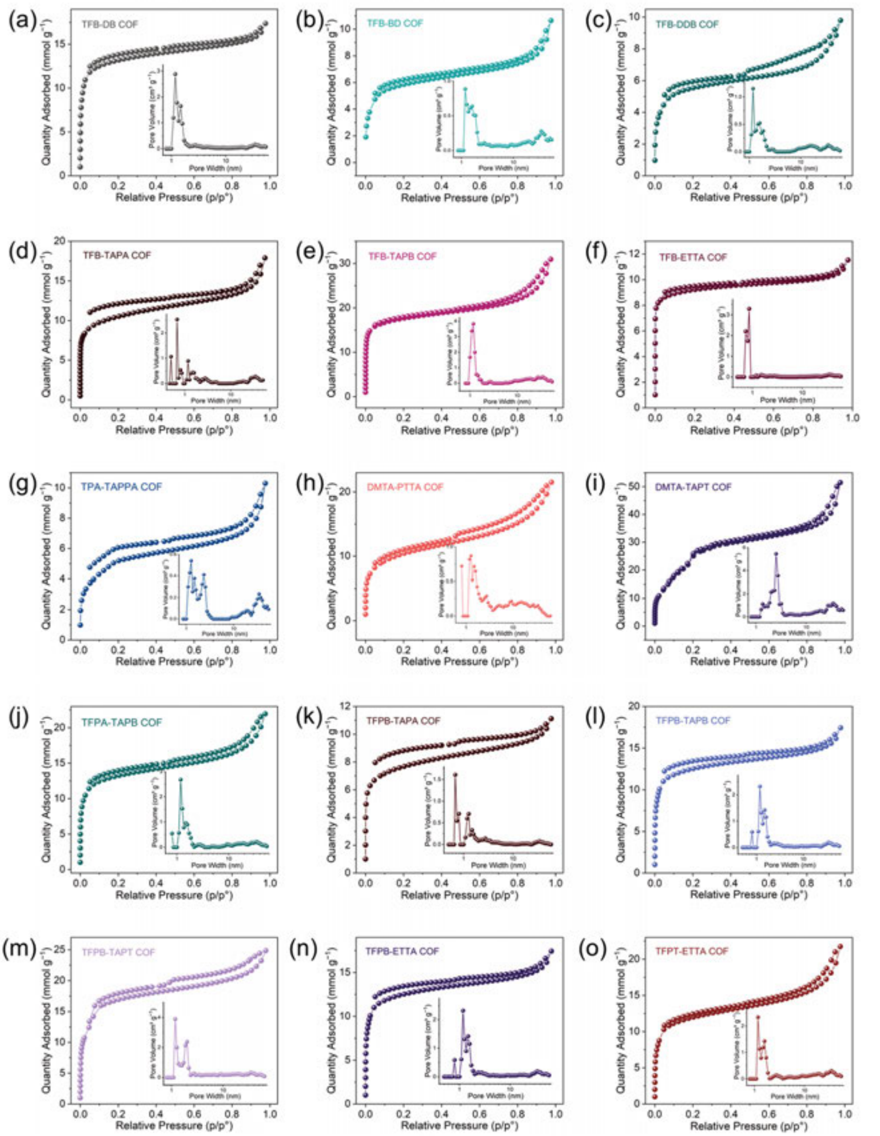

Figure 27 N_2 adsorption and desorption isotherms and pore size distributions (insert figures) of TDB-DB COF (a), TFB-BD COF (b), TFB-DDB COF (c), TFB-TAPA COF (d), TFB-TAPB COF (e), TFB-ETTA COF (f), TPA-TAPPA COF (g), DMTA-TAPT COF (h), DMTA-PTTA COF (i), TFPA-TAPB COF (j), TFPB-TAPA COF (k), TFPB-TAPB COF (l), TFPB-TAPT COF (m), TFPB-ETTA COF (n) and TFPT-ETTA COF (o).[86] These figures are adopted from **Paper IV**. Copyright (2023), published by American Chemical Society under an open access CC-BY 4.0 license.

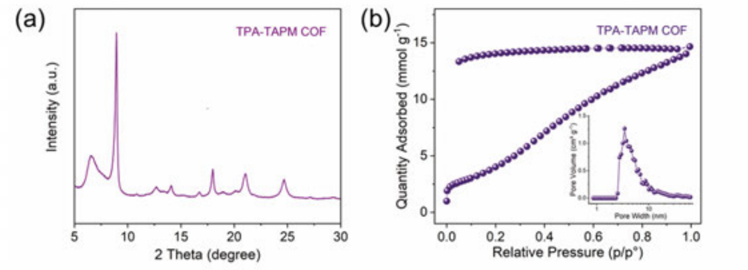

Figure 28 (a) XRD pattern and (b) N_2 adsorption and desorption isotherms and pore size distributions (insert figures) of TPA-TAPM COF.[86] These figures are adopted from **Paper IV**. Copyright (2023), published by American Chemical Society under an open access CC-BY 4.0 license.

In addition, we synthesized a 3D COF by reacting tetrakis(4-aminophenyl)methane (TAPM) with TPA. Interestingly, the reaction between TAPM and TPA using the AP method led to the formation of crystalline COF-300 (Figure 28a); however, two different crystalline phases (dia-c5 COF-300 and the hydrated form of COF-300) were identified in the obtained materials based on the XRD studies. Previous studies indicate that dia-c5 COF-300 exhibits a diamond (dia) topology with a 5-fold interpenetrated framework, giving it a high surface area of 1360 m^2 $g^{-1}$and rich microporosity.[60] In contrast, the hydrated form of COF-300 represents an isomer of dia-c5 COF-300 with a distorted structure and is nonporous.[92] The COF-300 sample obtained from AP method displays a moderate surface area of 305 m^2 g^{-1}, which agree with the fact that it contains mixed phases of the porous dia-c5 COF-300 and the nonporous hydrated form (Figure 28b).

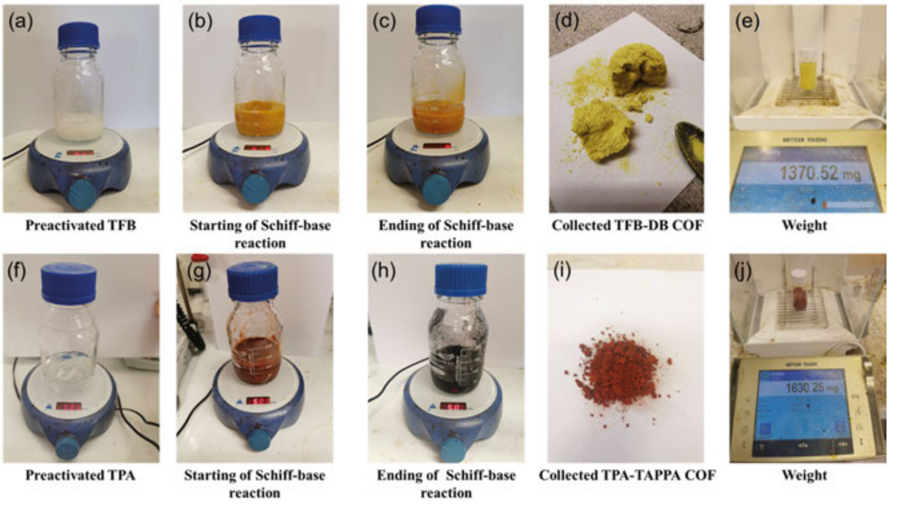

Figure 29 Optical images showing the gram-scale synthesis of TFB-DB COF (a-e) and TPA-TAPPA COF (f-j).[86] These figures are adopted from **Paper IV**. Copyright (2023), published by American Chemical Society under an open access CC-BY 4.0 license.

The AP method was further employed to achieve gram-scale synthesis of two imine-linked COFs, TFB-DB COF and TPA-TAPP COF (Figure 29). The collected imine-linked COFs also exhibit high crystallinity and BET surface area, indicating the feasibility of gram-scale synthesis (Figure 30).

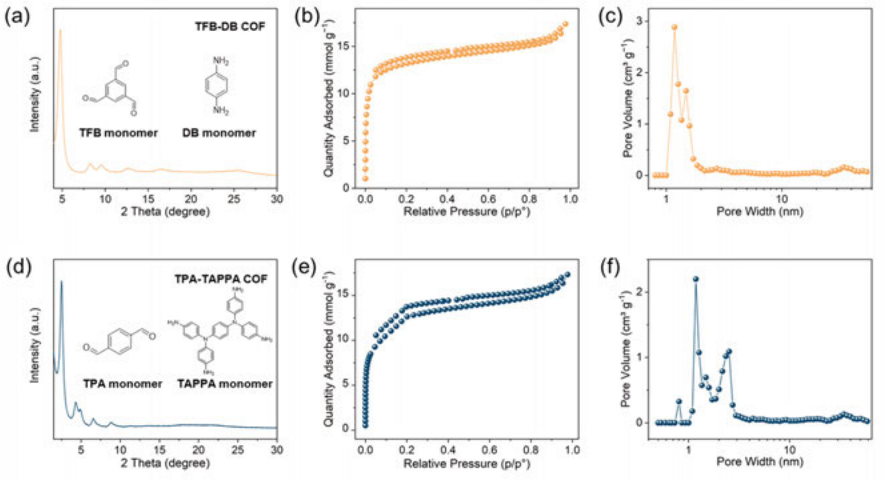

Figure 30 (a) XRD pattern, (b) N_2 adsorption-desorption isotherms, and (c) pore size distribution of TFB-DB COF obtained from the gram scale synthesis; (d) XRD pattern, (e) N_2 adsorption-desorption isotherms, and (f) pore size distribution of TPA-TAPPA COF obtained from the gram scale synthesis.[86] These figures are adopted from **Paper IV**. Copyright (2023), published by American Chemical Society under an open access CC-BY 4.0 license.

4. Fabrication and Characterization of Porous Materials Combined with *Cladophora* Cellulose Nanofiber

Most porous materials are insoluble and infusible powders, making them difficult to process and thereby limiting their practical applications. To address the poor processability, various substrates or templates (e.g. cellulose substrate,[93] glass substrate,[94] polytetrafluoroethylene substrates,[95] polyacrylonitrile template[57]) have been used to support porous materials and thus fabricated composite membranes. Among these substrates, cellulose is a promising material primarily because it is one of the most abundant renewable biopolymers on Earth. In particular, nanofibrillar cellulose, characterized by its nanofibrous structure and high aspect ratio, serves as an excellent substrate for porous materials. CNF extracted from *Cladophora* algae is particularly noteworthy, boasting a large aspect ratio (~ 4000), a high surface area (85 $m^2\ g^{-1}$), and remarkable crystallinity (> 95%). These properties endow it with exceptional mechanical strength and chemical stability, making it an ideal candidate for reinforcing materials in composites. Therefore, this chapter will introduce two strategies to integrate porous materials with CNFs in order to prepare freestanding nanopapers and aerogels.

4.1 Interweaving Porous Materials with *Cladophora* Cellulose Nanofiber

4.1.1 Fabrication and Properties of All-Cellulose-Based Porous Carbon (CC-CPC) Aerogel and CC-CPC Nanopaper

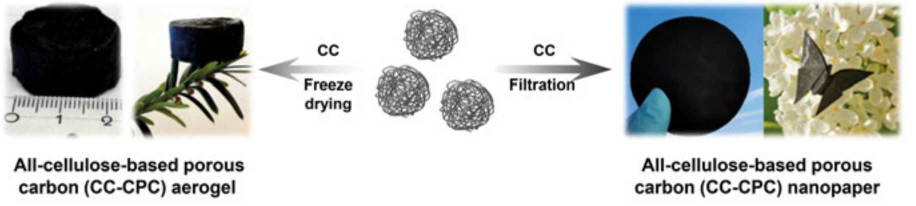

Figure 31 The formation of an all-cellulose-based porous carbon (CC-CPC) aerogel and CC-CPC nanopaper.[87] The figure is adopted from **Paper I**. Copyright (2021), published by Elsevier Ltd under an open access CC-BY license.

In **Paper I**, we utilized a sustainable biomass, specifically CC, as a carbon source to fabricate PC using a one-step physical carbonization/activation method. The obtained CPC was hydrophobic because the hydrophilic OH groups were removed during the pyrolysis process. The hydrophobic nature of CPC made it challenging to disperse in water, thereby limiting its applications. To address the hydrophobicity of CPC, we introduced hydrophilic COOH groups via acid treatment. As a result, the acid-treated CPC (a-CPC) exhibited good hydrophilicity and displayed excellent dispersion in water (Figure 14).

To improve the processability of a-CPC, we fabricated a homogeneous suspension of hydrophilic a-CPC and CC in a 1:1 mass ratio using a probe sonicator. This suspension was then processed into flexible nanopapers and free-standing aerogels through vacuum filtration and freeze-drying, respectively (Figure 31). The obtained nanopapers and aerogels were named CC-CPC nanopaper and CC-CPC aerogel, respectively.

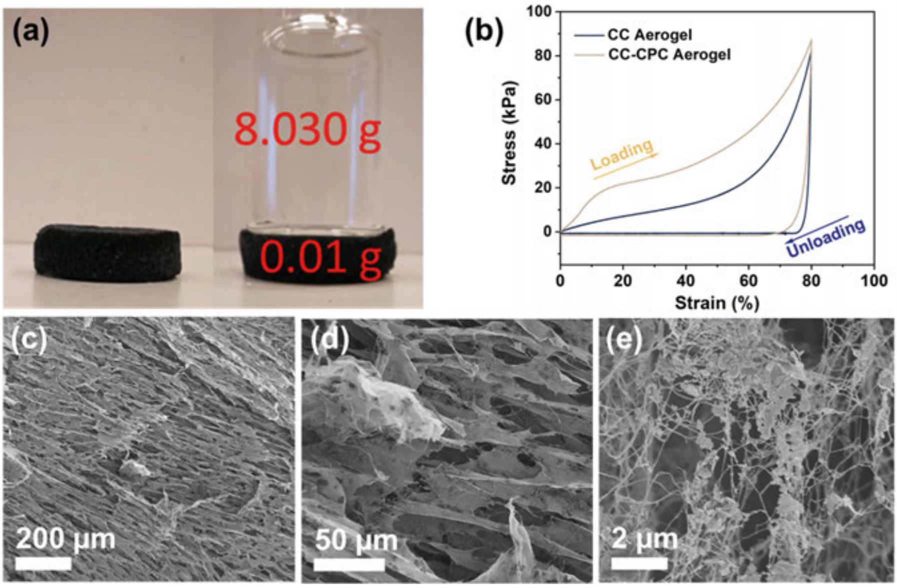

Figure 32 (a) The freestanding all-cellulose-based porous carbon (CC-CPC) aerogel and the sample loaded with a glass bottle; (b) compressive stress–strain curves for the CC aerogel and CC-CPC aerogel; SEM images of the CC-CPC aerogel showing the (c–d) cellular and (e) interweaving network.[87] These figures are adopted from **Paper I**. Copyright (2021), published by Elsevier Ltd under an open access CC-BY license.

The CC-CPC aerogel showed high elasticity, was capable of supporting a weight 803 times its own without significant deformation (Figure 32a). The high elasticity of CC-CPC aerogel can be attributed the cellular framework (Figures 32c-32d). The mechanical strength of the CC-CPC aerogel surpasses that of the pure CC aerogel (Figure 32b), which can be attributed to the reinforcement provided by uniformly distributed a-CPC particles within the cellular framework (Figures 32e). The CC-CPC aerogel possesses a high surface area of 237.6 m² g^{-1} and a hierarchical porous structure.

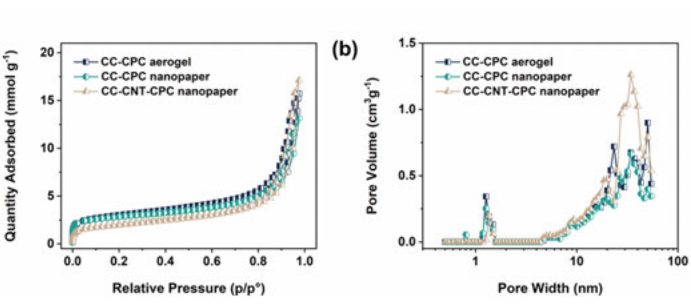

Figure 33 (a) N_2 adsorption and desorption isotherms of CC-CPC aerogel, CC-CPC nanopaper and CC-CNT-CPC nanopaper measured at 77K; (b) pore size distribution analyses of the nanopapers. These figures are adopted from **Paper I**. Copyright (2021), published by Elsevier Ltd under an open access CC-BY license.

The CC-CPC nanopaper with the same ratio of CC to a-CPC exhibits a surface area of 225.9 $m^2\ g^{-1}$ (Figure 33). The CC-CPC nanopaper also showed higher mechanical strength than pure CC nanopaper (Figure 34a), which is attributed to the homogenous distribution and interconnection of a-CPC particles within the CC network (Figures 34a-34c). Dense layered structures of CC-CPC nanopaper can be observed in the cross-sectional SEM images (Figures 34d-34f). These dense layered structures also contributed to reinforcing the mechanical strength of CC-CPC nanopaper.

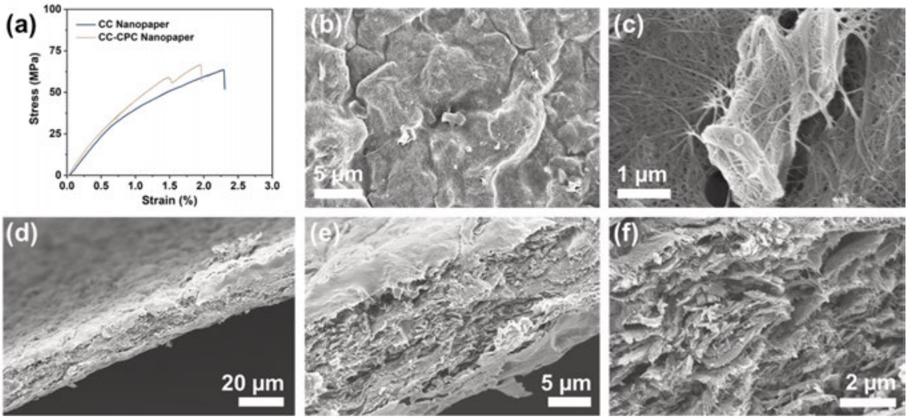

Figure 34 (a) Compressive stress–strain curves for the CC and CC-CPC nanopaper. SEM images of CC-CPC nanopaper taken from (b-c) the surface and (d-f) the cross-section.[87] These figures are adopted from **Paper I**.

4.1.2 Fabrication and Properties of c-CNT@COF/CNT/CNF Nanopaper

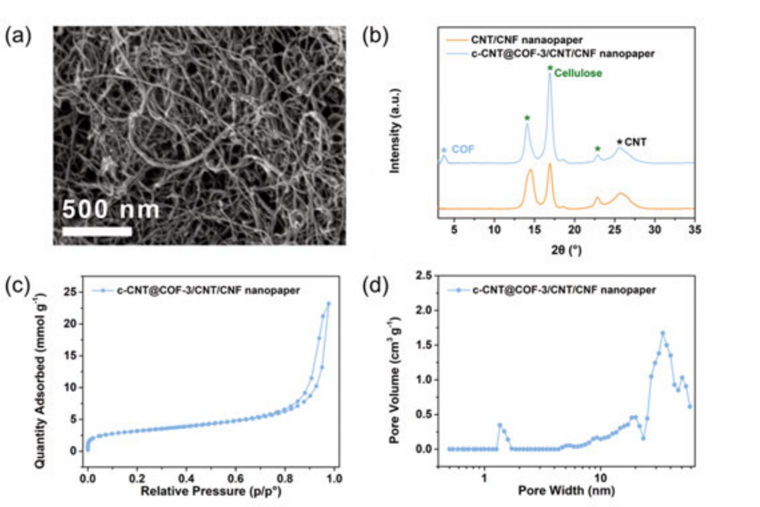

Figure 35 SEM image (a), XRD pattern (b), N_2 adsorption and desorption isotherm (c), and pore size distribution (d) of c-CNT@COF-3/CNT/CNF nanopaper.[88] These figures are adopted from **Paper III**. Copyright (2020), published by Elsevier Ltd under an open access CC-BY license.

The c-CNT@COF-3 nanofiber has excellent electrochemical performances, including high capacitance, a conductive core, and efficient utilization of redox active sites. To improve the processability of the c-CNT@COF-3 nanofiber and facilitate its use in flexible energy storage devices, we used c-CNT@COF-3 nanofibers as electrochemical active materials, combined with CNF as a flexible substrate and CNT as an additional conductive bridge to construct freestanding and flexible nanopaper electrodes (more information provided in **Paper III**). The mass ratio of the resultant c-CNT@COF-3/CNT/CNF nanopaper was 5:5:2. SEM imaging revealed a uniformly interlaced nanostructure comprising c-CNT@COF-3 nanofibers, CNF, and CNTs (Figure 35a). XRD analysis confirmed the presence of COF, CNF, and CNT components within the nanopaper (Figure 35b). N_2 sorption analysis revealed hierarchical structures, comprising both micropores and mesopores, with a high surface area of 331.8 m^2 g^{-1} (Figures 35c-35d). The micropores are inherited from the COF, while the formation of mesoporous structure can be attributed to the interweaving of nanofibers.

4.2 Interfacial Synthesis of *Cladophora* Cellulose Nanofiber @ Porous Materials

CNF with high crystallinity exhibits abundant surface functional groups that can be post-modified to obtain useful functional groups, such as carboxyl groups. In **Paper II and IV**, pristine CNFs were treated by TEMPO oxidation to introduce carboxyl groups. After oxidation, we used an interfacial synthesis method to fabricate CNF@MOF and CNF@COF nanocomposites and filtered them into freestanding nanopapers to address the challenges associated with processing MOFs and COFs.

4.2.1 Fabrication and Properties of CNF@Ni-HITP MOF Nanopaper

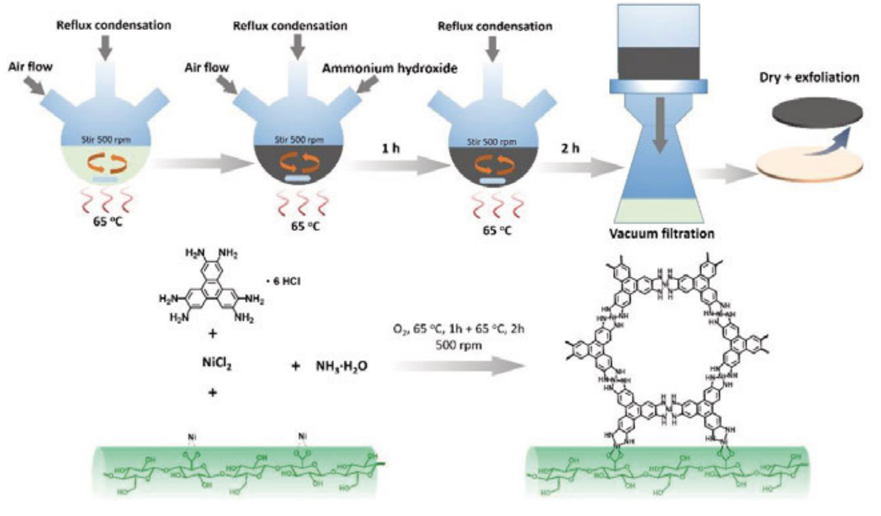

Figure 36 Schematic of the synthesis of the CNF@Ni-HITP MOF hybrid nanofiber and the procedures for preparing the CNF@Ni-HITP MOF nanopaper.[96] The figure is adopted from **Paper II**. Copyright (2022), published by American Chemical Society under an open access CC-BY 4.0 license.

To enhance the processability of Ni-HITP MOF, we introduced an interfacial synthesis method for preparing CNF@Ni-HITP MOF nanofibers in an aqueous solution (Figure 36, more information provided in **Paper II**). In this process, an aqueous solution of $NiCl_2$ was stirred with carboxylated CNFs. This process ensured that the surface of the CNFs was sufficiently coated with Ni(II) ions, which served as bridging sites to facilitate the combination of CNFs and MOFs. Consequently, the Ni-HITP MOF was able to fully wrap the surface of the carboxylated CNFs, resulting in the formation of nanofibrous structures (Figures 37a-37b). The resultant CNF@Ni-HITP MOF nanofibers were dispersed in water to form an aqueous suspension. This suspension was then processed into freestanding nanopaper via a vacuum filtration and drying procedure (Figure 36).

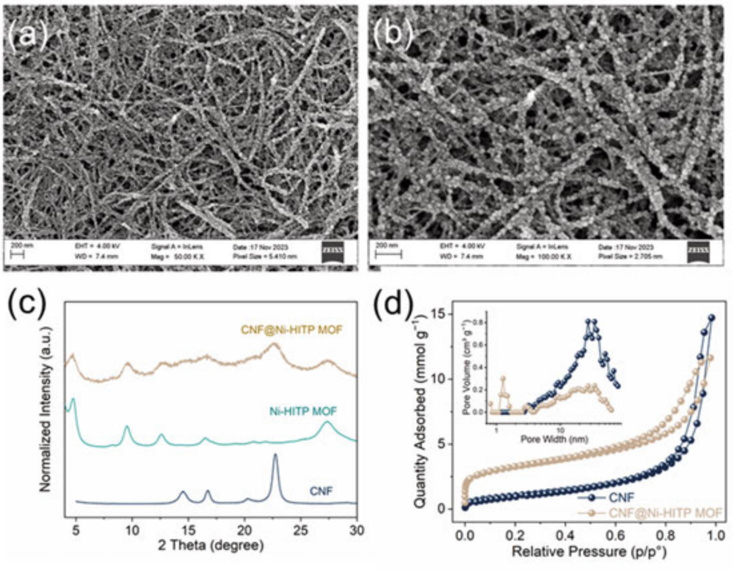

Figure 37 SEM images of CNF@Ni-HITP MOF hybrid nanofiber (a and b); XRD patterns of CNF, Ni-HITP MOF, and CNF@Ni-HITP MOF (c); N_2 adsorption and desorption isotherm and pore size distribution (d) of CNF and CNF@Ni-HITP MOF.

To confirm that Ni-HITP MOF has wrapped on the surface of carboxylated CNFs, we compared the diameters of the obtained hybrid nanofibers with that of pure CNF. As illustrated in Figures 37a-37b, the hybrid nanofibers are approximately 100 nm in diameter, significantly larger than that of pure CNF (≈ 20 nm, Figure 15a-15b). Furthermore, XRD analysis of the hybrid nanofibers revealed characteristic peaks at $2\theta \approx 4.7°$ and 9.5°, corresponding to the (100) and (200) planes of Ni-HITP MOF, and additional peaks at $2\theta \approx 13.1°$, 15.2°, 20.2°, corresponding to the (100), (010), and (110) planes of CNF, respectively (Figure 37c). These results indicate that a Ni-HITP MOF layer has successfully grown on the surface of the carboxylated CNFs to form CNF@Ni-HITP MOF nanofibers. Additionally, we processed CNF@Ni-HITP MOF nanofibers into CNF@Ni-HITP MOF nanopaper using a vacuum filtration and drying procedure and evaluated its porosity. Compared to pure CNF nanopaper, the resulting CNF@MOFs nanopaper exhibited microporous structure, attributed by the Ni-HITP MOF, leading to a high specific surface area of 263 $m^2\ g^{-1}$. (Figure 37d). These results confirm the successful interfacial growth of Ni-HITP MOFs on carboxylated CNF surfaces.

4.2.2 Fabrication and Properties of CNF@COF Nanopapers

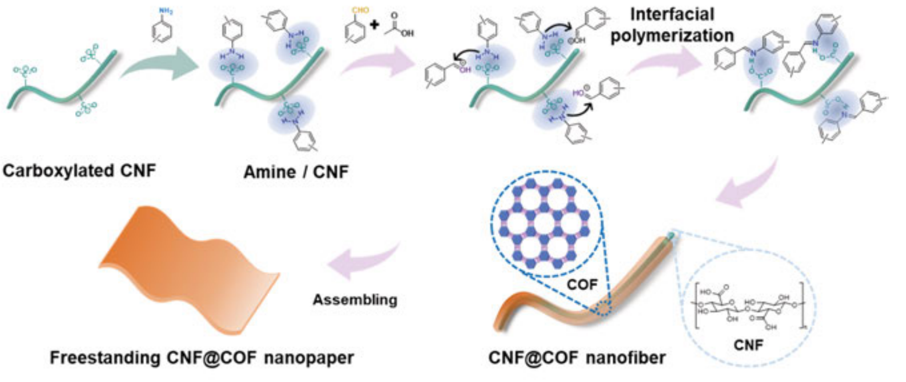

Figure 38 Illustration of synthesis of CNF@COF nanofibers and freestanding nanopapers.[86] The figure is adopted from **Paper IV**. Copyright (2023), published by American Chemical Society under an open access CC-BY 4.0 license.

In **Paper IV**, we developed a new strategy for the synthesis of imine-linked COFs in aqueous solution, which provides possibility for grow imine-linked COFs on the surface of carboxylated CNF to improve their processability. As shown in Figure 38, an aqueous carboxylated CNFs suspension was initially blended with amine monomers and stirred for one hour. Subsequently, acid-activated aldehyde monomers were introduced to this aqueous mixture under ambient conditions. Following the interfacial polymerization, we obtained CNF@COF nanofiber, which can be dispersed in water to form a uniform suspension. The suspension can be processed into freestanding CNF@COF nanopapers via a vacuum filtration and drying process.

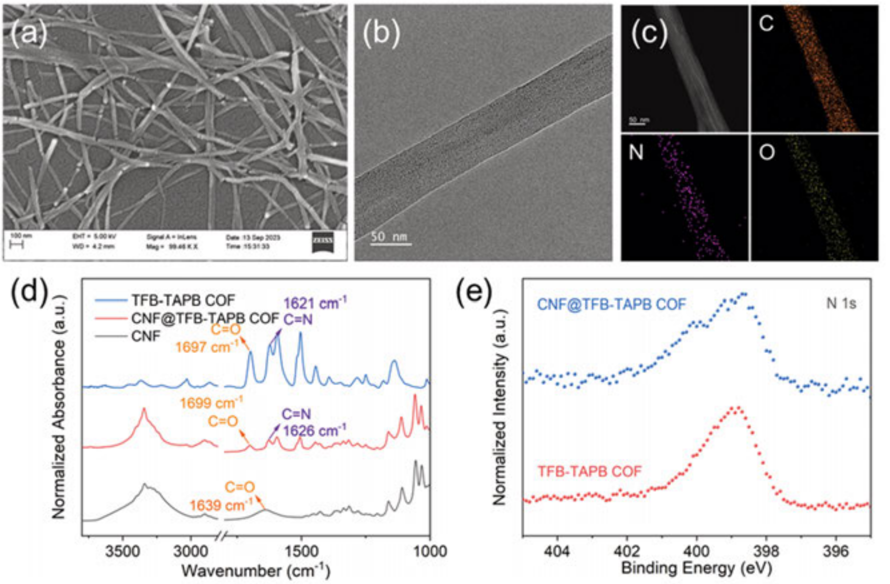

Figure 39 SEM image (a), TEM image (b), and energy-dispersive X-ray spectroscopy mapping (c) of CNF@TFB-TAPB COF nanofiber; IR spectra of CNF, TFB-TAPB COF, and CNF@TFB-TAPB COF (d); N 1s XPS spectrum for TFB-TAPB COF and CNF@TFB-TAPB COF (e).[86] These figures are adopted from **Paper IV.** Copyright (2023), published by American Chemical Society under an open access CC-BY 4.0 license.

We have successfully synthesized three distinct CNF@COFs: CNF@TFB-DB COF, CNF@TFB-TAPB COF, and CNF@TFB-ETTA COF (more information provided in **Paper IV**). Focusing on CNF@TFB-TAPB COF as an illustrative example, the SEM and TEM images clearly revealed the nanofibrous structures of CNF@TFB-TAPB COF (Figures 39a-39b). The diameters of CNF@TFB-TAPB COF nanofibers are around 70 nm, significantly larger than those of CNF (≈ 20 nm), as illustrated in Figures 15b and 39b. Additionally, the result from energy-dispersive X-ray spectroscopy mapping clearly shows the presence of N elements, which are found only in amine or imine bonds and are absent in CNF (Figure 39c). The XRD pattern of CNF@TFB-TAPB COF shows the characteristic peaks of both TFB-TAPB COF and CNF (Figure 40b), confirming that crystalline TFB-TAPB COF has been successfully grown on the surface of carboxylated CNFs. Compared with pure TFB-TAPB COF, we can observe a notable shift in the C=N vibration frequency (5 cm^{-1}) in the IR spectrum. A new shoulder peak at 400.0 eV is observed in the N1s XPS spectrum of CNF@TFB-TAPB COF, which is absent in pure TFB-TAPB COF. These results indicate that the chemical environments of N in TFB-TAPB COF have been changed upon the surface of carboxylated CNF, which can be attributed to the interaction between imine bonds and carboxyl (Figure 38). Meanwhile, these results demonstrate the carboxylated groups on CNFs play an important role in the fabrication of CNF@COF nanofibers.

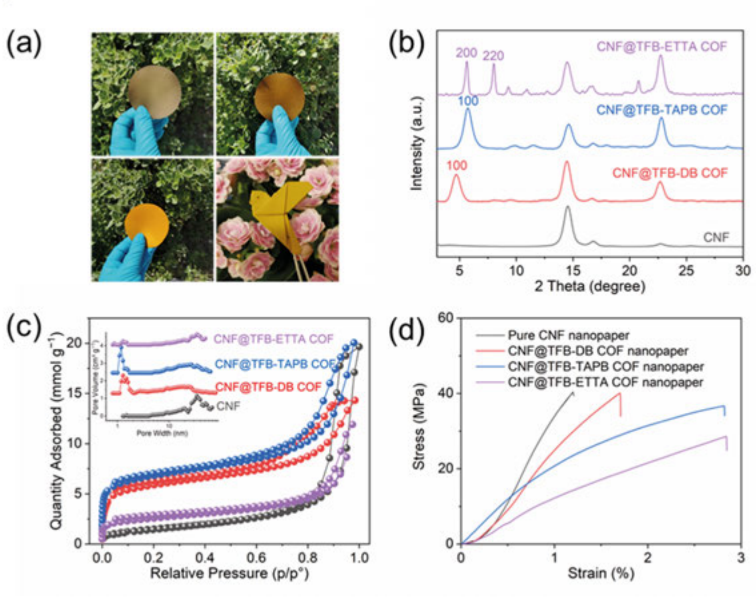

Figure 40 (a) Optical images of CNF@TFB-DB COF, CNF@TFB-TAPB COF, and CNF@ETTA COF nanopapers; XRD patterns (b), N_2 adsorption and desorption isotherm and pore size distribution (c) strain-stress curves (d) of pure CNF and CNF@COF nanopapers.[86] These figures are adopted from **Paper IV**. Copyright (2023), published by American Chemical Society under an open access CC-BY 4.0 license.

The obtained CNF@COFs inherited the nanofiber structure of CNF and could be dispersed into water to form a suspension, which inspired us to process the suspension into freestanding and flexible CNF@COF nanopaper via vacuum filtration and drying. As shown in Figure 40a, we have successfully prepared three freestanding CNF@COF nanopapers. The BET surface area of CNF@COFs ranged from 205 to 549 m^2 g^{-1} and exhibited microporous and mesoporous structures (Figure 40c). Mechanical testing of CNF@COF nanopapers showed high tensile strength and Young's moduli, reaching up to 40.2 MPa and 2.6 GPa, respectively (Figure 40d). This high mechanical strength is attributed to the interwoven nanofibrous structure and the high crystallinity of both CNF and COF.

5. Applications of Porous Materials Combined with *Cladophora* Cellulose Nanofiber

5.1 Electrochemical Energy Storage

5.1.1 Flexible Supercapacitor

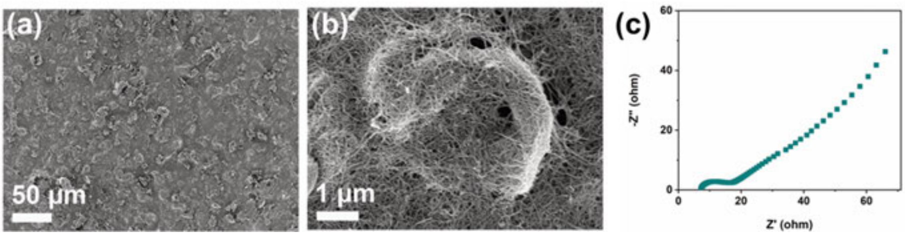

Figure 41 SEM images of CC-CNT-CPC nanopaper (a-b) and electrochemical impedance spectrum of CC-CNT-CPC nanopaper (c).[87] These figures are adopted from **Paper I**. Copyright (2021), published by Elsevier Ltd under an open access CC-BY license.

PC is a promising material for supercapacitor because of its high conductivity and high BET surface area. Additionally, the widespread development of flexible and wearable electronic devices has inspired us to process a-CPC and CC into flexible electrodes for supercapacitors. Specifically, a-CPC, CC, and multi-walled CNTs were assembled into a freestanding CC-CNT-CPC nanopaper, featuring a densely interconnected network (Figures 41a-41b). The nanopaper had a high surface area of 157.2 m^2 g^{-1}, and abundant micropores and mesopores (Figure 33). The added CNTs served as conductive pathways among the carbon nanoparticles, thereby enhancing the conductivity of nanopaper. As demonstrated in Figure 41c, the CC-CNT-CPC nanopaper exhibited low charge transfer resistance, ensuring fast charge transfer facilitated by the CNT conductive bridges. Furthermore, the low high-frequency resistance observed in the electrochemical impedance spectrum indicated efficient electrolyte transmission, attributed to the hierarchical porous structure of the CC-CNT-CPC nanopaper.

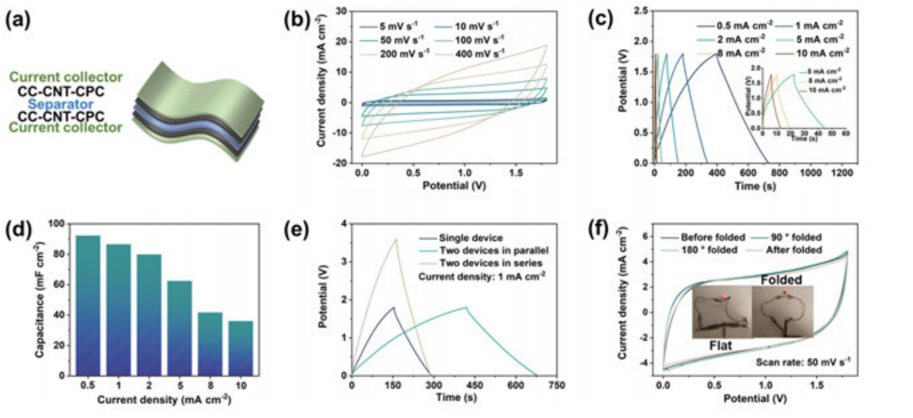

Figure 42 (a) Schematic illustration of the flexible supercapacitor; (b) cyclic voltammetry (CV) curves of the device at different scan rates; (c) galvanostatic charge and discharge (GCD) curves of the device at different current densities; (d) rate performance of the device at different current densities; (e) GCD curves of the assembled devices in parallel and series; (f) CV curves of the device under different folding conditions. The insert shows the LED powered by the flexible device. CC = *Cladophora* cellulose; CNT = carbon nanotubes; CPC = cellulose-derived porous carbons.[87] These figures are adopted from **Paper I**. Copyright (2021), published by Elsevier Ltd under an open access CC-BY license.

CC-CNT-CPC nanopaper displayed high surface area and excellent electrochemical performance, such as low charge transfer resistance and high-frequency resistance, demonstrating its potential for electrochemical applications. Subsequently, we assembled the CC-CNT-CPC nanopaper into flexible symmetrical supercapacitors in a coffee-bag arrangement (Figure 42a), in which the separator was a filter paper soaked in a 3 M KCl aqueous solution. The capacitance of the supercapacitor reached up to 92.3 mF cm^{-2} at current densities of 0.5 mA cm^{-2} (Figure 42c and 42d). Additionally, the supercapacitor showed a good rate capability, with 93.8%, 67.8%, and 39.1% of the capacitances retained at current densities of 1, 5, and 10 mA cm^{-2}, respectively. Additionally, devices configured in series and parallel showed good performance at 1 mA cm^{-2} (Figure 42e). The red LED was powered by two devices in series both before and after folding (Figure 42f), demonstrating the potential for powering flexible and wearable electronics.

5.1.2 Flexible Hybrid Capacitor

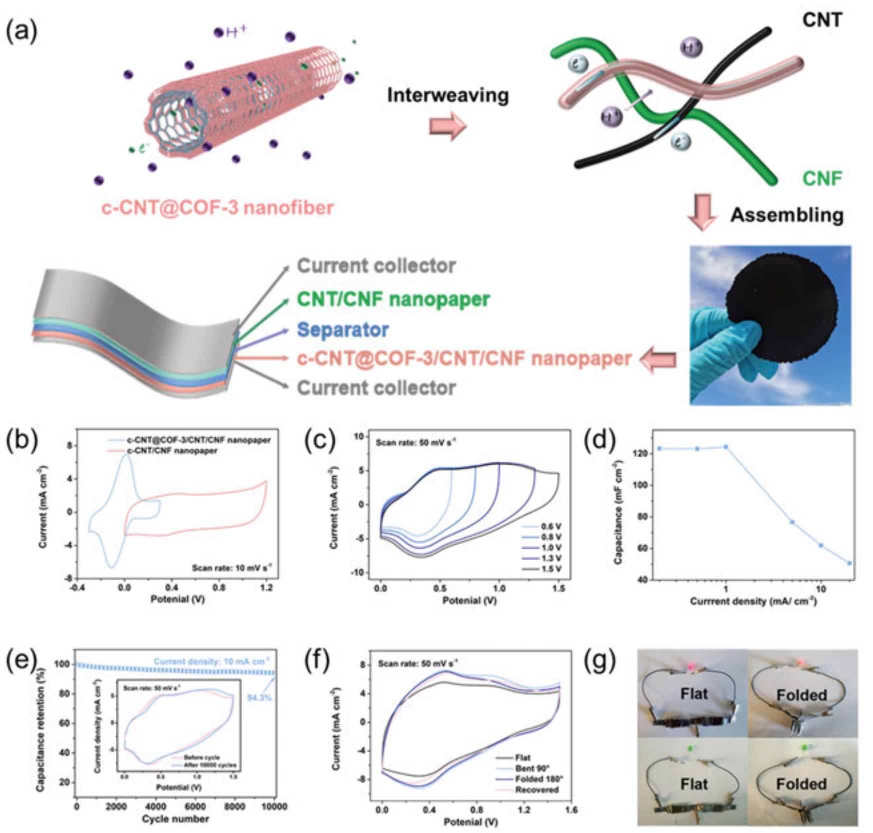

Figure 43 (a) Illustration of the flexible c-CNT@COF-3/CNT/CNF nanopaper and the assembled hybrid capacitor; (b) cyclic voltammetry (CV) curves of the c-CNT@COF-3/CNT/CNF and CNT/CNF nanopaper electrodes recorded in a three-electrode setup at a scan rate of 10 mV s^{-1}; (c) CV curves of the hybrid capacitor at different potential windows at the same scan rate of 50 mV s^{-1}; (d) areal capacitance and rate performance of the device; (e) cycling performance of device (the inset shows the CV curves of the device before and after the cycling experiment) (h) CV curves of device under different deformations; (g) photo of red and green LEDs powered by the flat or folded devices.[88] These figures are adopted from **Paper III**.

Given the high capacitance of c-CNT@COF-3 and its unique nanofibrous structure, we integrated it with CNT and CNF to form a freestanding and flexible nanopaper, which was used as an electrode in a flexible hybrid capacitor (Figure 43a). As shown in Figure 43b and 43c, the potential window of the capacitor can be extended to 1.5 V. The hybrid capacitor showed a high areal capacitance of 123.2 mF cm^{-2} at a current density of 0.2 mA cm^{-2} under low

COF loading (around 0.32 mg cm^{-2}) (Figure 43d). Additionally, the hybrid capacitor showed excellent rate capability (maintaining 100% and 41% capacitance under 5- and 100-times current density, respectively) and excellent cycling performance (retaining 94.3% capacitance after 10,000 GCD cycles). More importantly, as a flexible energy storage device, the hybrid capacitor exhibited excellent flexibility under working status, as shown in Figures 43f-43g, where the CV curves show no significant decrease under bending (90°) or folding (180°) and, both red and green LEDs were powered in the folded state.

The excellent performance of the hybrid capacitor can be attributed to the interwoven nanofibrous network, hierarchical porous structure, conductivity, crystalline structure, and high stability of the c-CNT@COF-3/CNT/CNF nanopaper. Specifically, the conductivity and interwoven structure of the hybrid capacitor ensure fast charge transfer and electrolyte ion diffusion during the charge/discharge processes. The high chemical stability yields excellent cycling performance, and the interwoven nanofibrous network provides flexibility and foldability.

5.2 Solar Thermal Energy Conversion

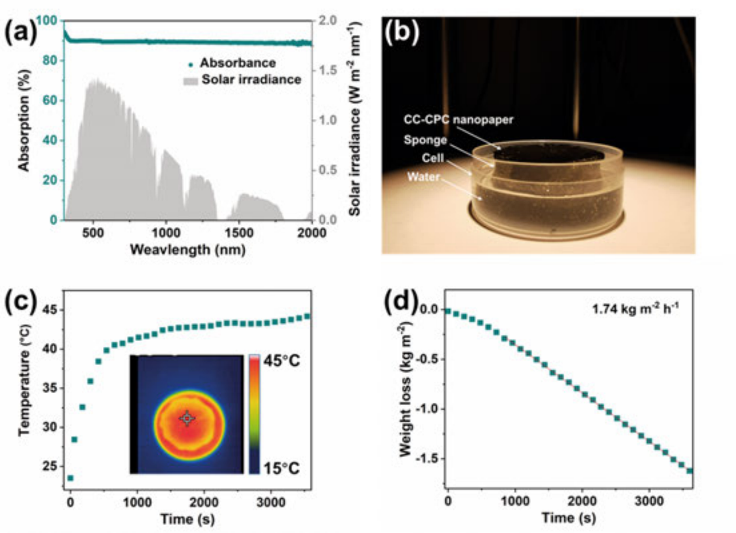

Figure 44 (a) Optical absorption of the all-cellulose-based porous carbon (CC-CPC) nanopaper in the region of the solar spectrum; (b) the interfacial solar vapor generator; (c) the time-dependent surface temperature on the CC-CPC nanopaper (the infrared image shows the temperature distribution on the surface of the nanopaper after being illuminated for 1 h); (d) the loss of water from the CC-CPC nanopaper under one sun illumination.[87] These figures are adopted from **Paper I**. Copyright (2021), published by Elsevier Ltd under an open access CC-BY license.

Carbon-based materials are highly efficient absorbers of solar energy and can effectively convert this solar energy into thermal energy. Figure 44a shows CC-CPC nanopapers exhibited strong broadband optical absorption across the solar spectrum (250–2000 nm). The excellent solar absorption motivated the use of freestanding CC-CPC nanopaper as a solar absorber in solar vapor generators. As shown in Figure 44b, the nanopaper was assembled with a sponge and a cell with bulk water to from a solar vapor generator. When exposed to a light with the intensity of one sun, the surface temperature of CC-CPC nanopaper rose up to 40°C in 10 minutes (Figure 44c). The vapor generation rate was calculated to be 1.74 kg m^{-2} h^{-1}, which surpassed the theoretical maximums of bulk water (1.47 kg m^{-2} h^{-1}) (Figure 44d). The enhanced evaporation rate is primarily due to the lower vaporization enthalpy of water within the confined nanopores structure as compared to that of bulk water. Concurrently, the low thermal conductivity of CC-CPC nanopaper (more information provided in **Paper I**), resulting from the separation of carbon nanoparticles by cellulose nanofibers, effectively minimized heat transfer from the carbon nanoparticles to the external environment. The uniform dispersion of a-CPC particles within the nanopaper promoted localized heating during the solar vapor generation process, while its porous, layered architecture, as evidenced in cross-sectional SEM images (Figure 34d-34f), enhanced water movement expediting the evaporation process.

5.3 Adsorption of CO_2 and Organic Solvents

5.3.1 CO_2 Adsorption

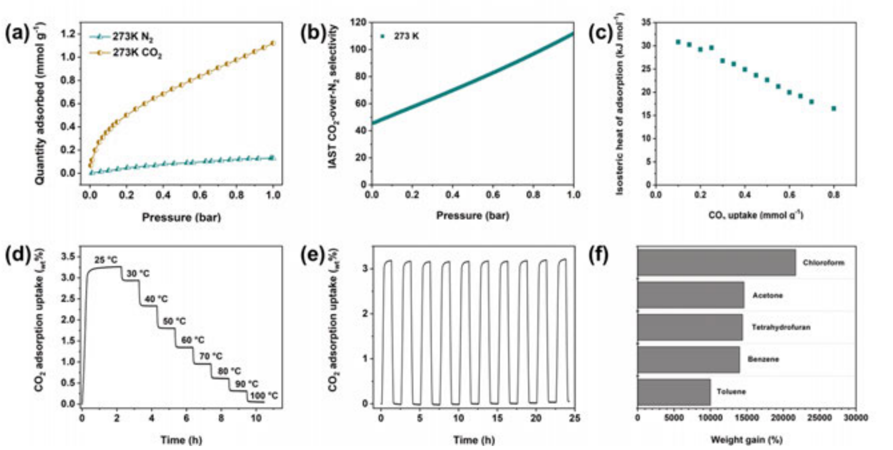

Figure 45 (a) CO_2 and N_2 adsorption isotherms for the all-cellulose-based porous carbon (CC-CPC) aerogel recorded at 273 K and 0–1 bar; (b) CC-CPC aerogel CO_2-over-N_2 selectivity calculated using ideal adsorbed solution theory (IAST) and the single-component CO_2 and N_2 adsorption isotherms recorded at 273 K; (c) isosteric heat adsorption of CO_2 calculated from the Clausius–Clapeyron equation; (d) gravimetric CO_2 adsorption isotherm recorded at 298 K and the desorption processes at elevated temperatures; (e) cyclic adsorption-desorption isotherms of the CC-CPC aerogel; (f) adsorption capacities of the aerogel for various organic liquids.[87] These figures are adopted from **Paper I**. Copyright (2021), published by Elsevier Ltd under an open access CC-BY license.

The CC-CPC aerogel has a rich hierarchical porous structure, including micropores and mesopores, which can be potentially utilized in adsorption and separation applications. To explore this, we used the CC-CPC aerogel as adsorbent to capture CO_2. The capacity of CC-CPC aerogel for CO_2 is significantly higher than N_2 (Figure 45a). Specifically, the capacity of CC-CPC aerogel for CO_2 can reach 0.44 mmol g^{-1} at 0.15 bar and 1.12 mmol g^{-1} at 1.0 bar. The IAST CO_2-over-N_2 selectivity was calculated as 111 under a mixed gas system (Figure 45b, more information provided in **Paper I).** The excellent selectivity of CC-CPC aerogel for CO_2 can be attributed to the molecular sieving effect from the ultra-micropores in a-CPC particles. Figure 45c reveals that the aerogel possesses a moderate isosteric heat of adsorption (Q_{st}) of 30.8 kJ mol^{-1} at lower coverage levels, suggesting a physisorption process for CO_2 adsorption (more information provided in **Paper I**). This characteristic indicates that the CC-CPC aerogel sorbent can be reactivated with a low energy consumption. Temperature swing adsorption was applied to assess the aerogel reactivation and the recyclability. As illustrated in Figure 45d, the capacity of CC-CPC aerogel for CO_2 adsorption was 3.27 wt% at 25°C, with 28.4%, 44.8%, and 70.7% of adsorbed CO_2 released upon heating to 40°C, 50°C, and

70°C, respectively. This result agrees with the moderate Q_{st}, indicating the low energy consumption for the reactivation of the aerogel sorbent. Additionally, the CC-CPC aerogel showed high stability and recyclability in CO_2 adsorption (Figure 45e).

5.3.2 Organic Solvents Adsorption

The freestanding CC-CPC aerogel exhibited high porosity and strong mechanical strength, making it a promising material for the removal of organic pollutant. To demonstrate this, the CC-CPC aerogel was immersed in different organic solvents to determine its adsorption capacity. By comparing the mass ratio of the aerogel before and after immersion, the adsorption capacity of the aerogel for organic solvents was determined. As illustrated in Figure 45f, the adsorption capacity for organic solvents can reach up to 217 times its own weight. The excellent adsorption capacity of the aerogel can be attributed to its high overall porosity (99.8%). Overall, the excellent adsorption capacity, high stability and good mechanical properties of the CC-CPC aerogels support their potential use as gas and organic solvent sorbent.

5.5 Adsorption of Antibiotic

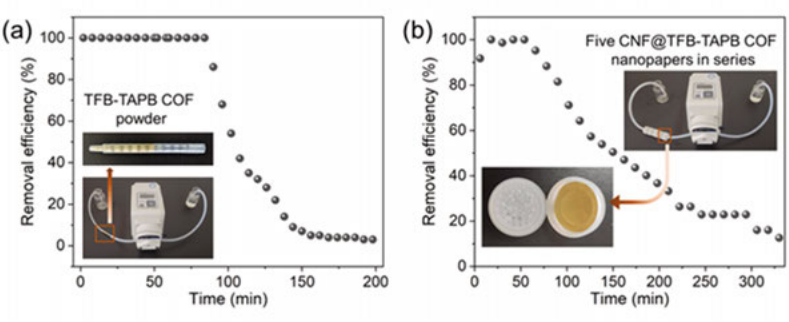

Figure 46 (a) Removal efficiency of TFB-TAPB COF powder for ofloxacin (OFX) from aqueous solution (10 ppm); and (b) removal efficiency of CNF@TFB-TAPB COF nanopapers for ofloxacin from aqueous solution (2 ppm).[86] These figures are adopted from **Paper IV**. Copyright (2023), published by American Chemical Society under an open access CC-BY 4.0 license.

The high surface area and abundant microporosity of COFs, coupled with their integration into CNF@COF nanopapers, make them exceptionally promising for wastewater treatment applications. Therefore, we utilize two adsorption devices to remove trace amounts of ofloxacin (OFX) from water. Specifically, we compared OFX removal at 10 ppm and 2 ppm using TFB-TAPB COF powder and CNF@TFB-TAPB COF nanopapers, respectively (Figure 46). 180 mg of TFB-TAPB COF was placed into a tube, and five CNF@TFB-TAPB COF nanopapers were arranged in series, with a total COF mass loading of 68.5 mg (more information provided in **Paper IV**). OFX aqueous solutions were passed through the samples at a flow rate of 0.17 mL min^{-1}.

The tube containing TFB-TAPB COF powder achieved a removal efficiency of 96.7% over the initial 80 minutes, indicating it is an efficient adsorbent. This high removal efficiency is attributed to the high surface area and rich microporous structure in TFB-TAPB COF. The five CNF@TFB-TAPB COF nanopapers similarly demonstrated good adsorption efficiency with approximately 100% removal of OFX within the initial 60 minutes (Figure 46b). Additionally, the CNF@TFB-TAPB COF nanopaper exhibited high mechanical strength (Figure 40d), facilitating its assembly into a filtration system and its recyclability after use. The CNF@TFB-TAPB COF nanopaper not only demonstrates ease of operation but also exhibits excellent adsorption and separation performance, indicating that it has great potential for the application of adsorption.

6. Summary

Porous materials are acknowledged to have significant potential in various applications, yet their widespread applications have been hampered by several challenges, such as poor processability and environmentally unfriendly synthesis. Additionally, the low electrical conductivity of many COFs limits their application in electrochemical energy storage. To overcome these issues, we investigated the synthesis, functionalization, processing and application of porous materials, including PCs, MOFs, and COFs.

We used CC, a biomass polymer, as a precursor to prepare PC via a one-step physical carbonization/activation method. During the process, the gaseous products (H_2O and CO_2) acted as activation agents and templates which ensure the formation of porous structures, thereby avoiding the utilization of other corrosive activating agents **(Paper I)**. The resulting CPC, with its high surface area, was further treated with acid to introduce hydrophilic COOH groups, enhancing its dispersibility in water. This hydrophilic a-CPC was interwoven with CC to produce freestanding nanopapers and aerogels, as sustainable carbon nanocomposites. Subsequently, CC-CPC aerogels were used for CO_2 capture and organic solvents removal, while the nanopaper served as heat absorber for solar vapor generation and as an electrode in flexible, foldable supercapacitors.

Furthermore, we introduced an interfacial synthesis method for the preparation of CNF@c-MOF nanofibers in aqueous conditions, which improved the processability of c-MOF (**Paper II**). The CNF@c-MOF suspension was easily processed into nanopaper, integrating these advantages of CNF and c-MOFs, including good conductivity, high surface area, rich microporous structure and flexibility. These properties show the great potential of CNF@c-MOF nanopaper in different applications, such as electrochemical energy storage, solar-driven ionic power generation, and solar vapor generation.

To overcome the low conductivity of COFs, we introduced an interfacial synthesis method to fabricate redox-active COFs (DAAQ-TFP COF) on the surface of c-CNTs, resulting in core-shell c-CNT@COF nanofiber **(Paper III)**. The c-CNT cores acted as a conductive skeleton, ensuring electron transfer along the nanofibers. Notably, we controlled the thickness of DAAQ-TFP

COFs layers on the c-CNTs via adjusting the mass ratio of COF and c-CNT. The obtained c-CNT@COF-3 with a few layers COF achieved a 99.1% utilization of the redox-active sites of COF in a three-electrode system. Furthermore, c-CNT@COF-3 was prepared into freestanding, flexible nanopaper by interweaving CNTs and CNFs. The additional CNTs acted as the conductive bridge among c-CNT@COF nanofibers. The obtained c-CNT@COFs/CNT/CNF nanopaper was used as a flexible electrode in flexible hybrid capacitors, which showed good electrochemical performance and flexibility.

Finally, we reported a simple and green synthesis strategy of imine-linked COFs and an interfacial synthesis strategy for CNF@COFs nanofibers in an aqueous solution (**Paper IV**). Notably, we found a key factor, regulating the reaction rate, which influenced the formation of crystalline imine-linked COFs in aqueous solution. By pre-activating aldehyde monomers with acetic acid, their reactivity in aqueous solution was significantly increased. This approach, in comparison to traditional solvothermal methods, results in a slower imine formation rate and a faster rate of imine breaking. This facilitates the adjustment of the equilibrium of reaction and the crystallization of the final products. Consequently, this method enables the production of highly crystalline TFB-DB COFs with high surface areas and relatively high yields within 1 minute. Additionally, we successfully obtained an additional 15 distinct imine-linked COFs, including 14 two-dimensional COFs and one three-dimensional COF. Furthermore, we used an interfacial synthesis strategy to grow COF nanolayers on carboxylated CNFs in aqueous solution. The resultant CNF@COF nanofibers were easily transformed into freestanding nanopapers, which could be used to effectively remove trace OFX from wastewater.

In this thesis, we have addressed some issues, that have limited the use of highly porous materials (PCs, MOFs, and COFs), such as poor processability of porous materials, environmentally unfriendly synthesis methods of PC and imine-linked COFs, and low conductivity of redox-active COF. However, there are still some challenges that remain for porous materials. For example, the fabrication of redox-active COFs used a lot of PTSA, a strong organic acid, which is environmentally hazardous. Additionally, 3D imine-linked COFs have not yet been synthesised on the surface of carboxylated CNFs, limiting their processability. In future work, we will aim to synthesize redox-active COFs by using our acid AP method, and avoid the heavy use of PTSA. Additionally, we will further construct functional CNF@COFs nanopapers for various applications, such as interfacial catalysis and solar vapor generation.

7. Sammanfattning

Porösa material har många lovande egenskaper som gör dem lämpliga för olika tillämpningar. Dock har den storskaliga appliceringen av dessa ämnen hindrats, framförallt på grund av deras låga bearbetningsförmåga och ohållbara framställningsprocess. Många material, mer specifikt kovalenta organiska ramverk (COF:ar), har dessutom en låg ledningsförmåga vilket begränsar deras användning för elektrokemisk energilagring. I denna avhandling har vi undersökt syntesen, funktionaliseringen, bearbetningen, samt tillämpningen av porösa material så som porösa kolmaterial (PC:ar), metallorganiska ramverk (MOF:ar) och COF:ar i syfte att hitta innovativa lösningar till dessa problem

Polymeren CC, erhållen från biomassa, användes som prekursor för att framställa ett poröst kol (CPC) genom en fysikalisk karboniserings/aktiveringsmetod **(Artikel I)**. Användandet av frätande aktiveringsmedel kunde undvikas då de gasformiga produkterna (H_2O och CO_2) som bildades under processen kunde agera både som aktiveringsmedel och mall för att skapa den porösa strukturen. Materialet modifierades därefter för att öka CPC:ens hydrofilicitet samt dispersion i vatten, varefter det hydrofila materialet (a-CPC) vävdes samman med cellulosananofibrer (CNF) för att skapa hållbara fristående kompositmaterial såsom nanopapper och aerogeler. Slutligen användes CC-CPC-aerogelerna för att fånga in organiska ämnen samt för koldioxidavskiljning medans nanopapprena kunde agera som ljusabsorberande material för soldriven generering av vattenånga samt användas som elektrodmaterial i flexibla superkondensatorer.

För att förbättra bearbetningen av c-MOF:ar utvecklades därefter en vattenbaserad gränsytesyntes från vilket CNF@c-MOF nanofibrer framställdes (**Artikel II**). Den erhållna suspensionen av CNF@c-MOF kunde lätt omvandlas till nanopapper som bibehöll de fördelaktiga egenskaper hos både MOF:arna och CNF:en, såsom god ledningsförmåga och flexibilitet, stor ytarea, samt mikroporös struktur. Dessa unika egenskaper gjorde CNF@c-MOF nanopapper lämpliga för många olika tillämpningar, exempelvis för elektrokemisk energilagring, soldriven och jon-baserad elgenerering, samt soldriven generering av vattenånga.

För att kringgå den låga ledningsförmågan hos många COF material så tillverkades en redoxaktiv COF (DAAQ-TFP COF) på ytan av karboxylerade kolnanorör (c-CNT) genom en ny gränsyte-baserad syntesmetod. Detta resulterade i kärn/skal-strukturerade c-CNT@COF nanofibrer (**Artikel III**) där c-CNT:en agerade som ett ledande skelett och säkerställde att elektronerna kunde röra sig genom fibrerna. Noterbart kontrollerade vi tjockleken på DAAQ-TFP COF:ar skikt på c-CNT:en genom att justera massförhållandet mellan COF och c-CNT. Det erhållna c-CNT@COF-3 med några lager COF uppnådde 99,1 % användning av de redoxaktiva platserna i COF i ett trecellelektrodssystem. Genom att sammanväva CNT och CNF framställdes därefter fristående och flexibla c-CNT@COF-3 nanopapper där ytterligare CNT:en agerade som en ledande brygga mellan c-CNT@COF nanofibrerna. De erhållna c-CNT@COF/CNT/CNT nanopapprena kunde därefter användas som elektroder i hybridkondensatorer som påvisade goda elektrokemiska egenskaper samt flexibilitet.

Slutligenf presenterades även en enkel och hållbar vattenbaserad syntesmetod för tillverkningen av iminlänkade COF:ar samt en gränsytesyntes för CNF@COF nanofibrer (**Artikel IV**). Noterbart fann vi en nyckelfaktor, reglering av reaktionshastigheten, som påverkade bildandet av kristallina iminlänkade COF:ar i vattenlösning. Genom att föraktivera aldehydmonomerer med ättiksyra ökades deras reaktivitet i vattenmiljöer avsevärt. Denna metod, jämfört med traditionella solvotermiska metoder, resulterar i en långsammare iminbildningshastighet och en snabbare hastighet för iminbrytning. Detta underlättar justeringen av reaktionens jämvikt och kristalliseringen av de slutliga produkterna. TFB-DB-COF:ar med hög kristallinitet och stor ytarea kunde därav erhållas med ett högt kemiskt utbyte inom 1 minut. Utöver detta kunde ytterligare 15 iminlänkade COF:ar erhållas, däribland 14 stycken 2D COF:ar samt en 3D COF. Komposit CNF@COF nanofibrer framställdes sedan genom att nanometer tjocka COF-lager växtes på ytan av karboxylerad CNF i en vattenlösning. De resulterande CNF@COF komposit nanofibrerna kunde lätt omvandlas till fristående nanopapper och sedan användas för att effektivt avlägsna antibiotika från avloppsvatten.

I denna avhandling har vi behandlat viktiga frågor som berör den låga bearbetningsförmågan hos många porösa material (t.ex. PC:ar, MOF:ar, och COF:ar), utvecklingen av hållbara syntesmetoder för PC och iminlänkade COF:ar samt den låga ledningsförmågan hos COF materialen. Trots de framsteg som åstadkommits så finns det fortfarande frågor och problem som kvarstår, t.ex. användes stora mängde PTSA, en stark miljöovänlig organisk syra, för att syntetisera de redoxaktiva COF:arna och framställningen av kompositmaterial från 3D iminlänkade COF:ar och karboxylerad CNF undersöktes ej. Framtida studier kommer därav att utreda syntesen av redoxaktiva COF:ar genom den föraktiverade syra-baserade syntesmetoden där PTSA ej behöver tillsättas samt tillverkningen och bearbetningen av funktionella CNF@COF nanopapper för olika tillämpningar såsom soljusdriven generering av vattenånga och katalys.

8. Acknowledgements

Throughout my academic journey, I have been profoundly touched by the selfless support and assistance provided by my supervisors. At this moment, I would like to express my special gratitude to Chao Xu and Maria Strömme. They have not only been supervisors for my scholarly exploration but also steadfast friends who supported me through challenging times. I wish to convey my deepest appreciation to Chao. Chao has been instrumental in my academic development, offering invaluable guidance that has propelled me forward in the field of porous materials. More than that, during moments of challenge, his extensive experience and insightful perspectives have directed me towards solutions. Chao's rigorous academic demeanour and relentless pursuit of knowledge have deeply influenced me, motivating me to persevere. I am exceedingly grateful to Maria, who has played a pivotal role in both my academic research and personal growth. Her passion for work has profoundly inspired and encouraged me. Moving forward, I will transform this gratitude into motivation, continuing to strive tirelessly on both the academic research and life paths ahead.

Since joining our NFM, I have received warm support from all my colleagues, to whom I owe a great deal of thanks for their assistance in my research and their support in my work throughout this learning journey. Special thanks to Michelle for helping me correct the summary in Swedish. I extend my gratitude to Anna, Daniel, Felicia, Jonas, Johan, Kasper, Ken, Martin, Maxim, Natalia, Ocean, Oleg, Philipp, Rebecka, Serena, Tyran, Teresa, and Valerie. I am very happy to that I could work with all of you together.

I'd like to extend my heartfelt gratitude to the friends I made in Sweden. Even though some have since departed from Sweden, there are still friends who remain by my side. I am truly grateful for the wonderful moments we've shared together. We've journeyed, explored trails, marvelled at the aurora, admired cherry blossoms, witnessed both sunrise and sunset, savoured the sea breeze, endured sudden rain showers, indulged in poker and mahjong, and shared countless delicacies. Thank you, my friends, Huan Wang, Rui Sun, Lei Tian, Jie Zhao, Xingxing Xu, Xi Chen, Shuangshuang Zeng, Jiaqi Lu, Shengyang Zhou, Qitao Hu, Shiyu Li, Pei Fu, Yingtao Yu, Linglu Hong, Zheqiang

Xu, Jing Xu, Yuan Cui, Qian Shi, Funing Liu, Chencheng Liang, Shan Jiang, Yu Pan, Yihan Wang.

感谢徐晓阳和周玮，感谢你们跨越时差和距离一直陪伴着我度过所有难忘的时刻。时间为证，岁月为名，友谊万岁。
感谢祝渊，感谢你与我分享你的岁月与人生。往后日子，窗外阳光依旧灿烂，时光漫漫，生活漫漫，和你漫漫。
感谢我的妈妈，感谢你对我的无限包容，毫无保留的支持和历久弥新的爱。感谢我的爸爸，感谢你对我的培养和付出，在这一刻我想告诉你，我距离完成我们的约定又近了一步。感谢我的弟弟，感谢你对我的挂念和支持。
纵有千古，横有八荒。前途似海，来日方长。

孔雪莹
2024 年 4 月 8 日于乌普萨拉
Xueying Kong
20240408, Uppsala

9. References

1. Rouquerol, J.; Avnir, D.; Fairbridge, C. W.; Everett, D. H.; Haynes, J. M.; Pernicone, N.; Ramsay, J. D. F.; Sing, K. S. W.; Unger, K. K., Recommendations for the characterization of porous solids (Technical Report). **1994,** *66* (8), 1739-1758.
2. Wu, Z. Y.; Li, C.; Liang, H. W.; Chen, J. F.; Yu, S. H., Ultralight, flexible, and fire-resistant carbon nanofiber aerogels from bacterial cellulose. *Angewandte Chemie International Edition* **2013,** *52* (10), 2925-2929.
3. Zhou, W.; Wang, X.; Zhao, W.; Lu, N.; Cong, D.; Li, Z.; Han, P.; Ren, G.; Sun, L.; Liu, C.; Deng, W. Q., Photocatalytic CO(2) reduction to syngas using metallosalen covalent organic frameworks. *Nature Communications* **2023,** *14* (1), 6971.
4. Li, Y.; Wu, Q.; Guo, X.; Zhang, M.; Chen, B.; Wei, G.; Li, X.; Li, X.; Li, S.; Ma, L., Laminated self-standing covalent organic framework membrane with uniformly distributed subnanopores for ionic and molecular sieving. *Nature Communications* **2020,** *11* (1), 599.
5. Zhao, S.; Jiang, C.; Fan, J.; Hong, S.; Mei, P.; Yao, R.; Liu, Y.; Zhang, S.; Li, H.; Zhang, H.; Sun, C.; Guo, Z.; Shao, P.; Zhu, Y.; Zhang, J.; Guo, L.; Ma, Y.; Zhang, J.; Feng, X.; Wang, F.; Wu, H.; Wang, B., Hydrophilicity gradient in covalent organic frameworks for membrane distillation. *Nature Materials* **2021,** *20* (11), 1551-1558.
6. Nam, K. W.; Park, S. S.; Dos Reis, R.; Dravid, V. P.; Kim, H.; Mirkin, C. A.; Stoddart, J. F., Conductive 2D metal-organic framework for high-performance cathodes in aqueous rechargeable zinc batteries. *Nature Communications* **2019,** *10* (1), 4948.
7. Huang, R.; Cao, C.; Liu, J.; Sun, D.; Song, W., N-Doped carbon nanofibers derived from bacterial cellulose as an excellent metal-free catalyst for selective oxidation of arylalkanes. *Chemical Communications* **2019,** *55* (13), 1935-1938.
8. Mu, P.; Zhang, Z.; Bai, W.; He, J.; Sun, H.; Zhu, Z.; Liang, W.; Li, A., Superwetting monolithic hollow-carbon-nanotubes aerogels with hierarchically nanoporous structure for efficient solar steam generation. *Advanced Energy Materials* **2018,** *9* (1), 1802158.
9. Li, S. C.; Hu, B. C.; Ding, Y. W.; Liang, H. W.; Li, C.; Yu, Z. Y.; Wu, Z. Y.; Chen, W. S.; Yu, S. H., Wood-derived ultrathin carbon nanofiber aerogels. *Angewandte Chemie International Edition* **2018,** *57* (24), 7085-7090.
10. Li, S.; Warzywoda, J.; Wang, S.; Ren, G.; Fan, Z., Bacterial cellulose derived carbon nanofiber aerogel with lithium polysulfide catholyte for lithium–sulfur batteries. *Carbon* **2017,** *124*, 212-218.
11. Singh, G.; Lakhi, K. S.; Sil, S.; Bhosale, S. V.; Kim, I.; Albahily, K.; Vinu, A., Biomass derived porous carbon for CO2 capture. *Carbon* **2019,** *148*, 164-186.

12. De, Q.; Xu, X., Building polyoxometalate "nano-walls" on 3D porous carbon paper: a solar steam generation system for water purification. *Chemistry—A European Journal* **2020,** *26* (35), 7923-7929.
13. Yin, J.; Zhang, W.; Alhebshi, N. A.; Salah, N.; Alshareef, H. N., Synthesis Strategies of porous carbon for supercapacitor applications. *Small Methods* **2020,** *4* (3), 1900853.
14. Sevilla, M.; Diez, N.; Fuertes, A. B., More sustainable chemical activation strategies for the production of porous carbons. *ChemSusChem* **2021,** *14* (1), 94-117.
15. wang, L.; Zhang, Z.; Qu, Y.; Guo, Y.; Wang, Z.; Wang, X., A novel route for preparation of high-performance porous carbons from hydrochars by KOH activation. *Colloids and Surfaces A: Physicochemical and Engineering Aspects* **2014,** *447*, 183-187.
16. He, X.; Ling, P.; Qiu, J.; Yu, M.; Zhang, X.; Yu, C.; Zheng, M., Efficient preparation of biomass-based mesoporous carbons for supercapacitors with both high energy density and high power density. *Journal of Power Sources* **2013,** *240*, 109-113.
17. Guo, Y.; Qi, J.; Jiang, Y.; Yang, S.; Wang, Z.; Xu, H., Performance of electrical double layer capacitors with porous carbons derived from rice husk. *Materials Chemistry and Physics* **2003,** *80* (3), 704-709.
18. Prauchner, M. J.; Rodríguez-Reinoso, F., Chemical versus physical activation of coconut shell: a comparative study. *Microporous and Mesoporous Materials* **2012,** *152*, 163-171.
19. Kim, D.-W.; Kil, H.-S.; Nakabayashi, K.; Yoon, S.-H.; Miyawaki, J., Structural elucidation of physical and chemical activation mechanisms based on the microdomain structure model. *Carbon* **2017,** *114*, 98-105.
20. Lee, J.; Kim, J.; Hyeon, T., Recent progress in the synthesis of porous carbon materials. *Advanced Materials* **2006,** *18* (16), 2073-2094.
21. Chen, C.; Zhang, Y.; Li, Y.; Dai, J.; Song, J.; Yao, Y.; Gong, Y.; Kierzewski, I.; Xie, J.; Hu, L., All-wood, low tortuosity, aqueous, biodegradable supercapacitors with ultra-high capacitance. *Energy & Environmental Science* **2017,** *10* (2), 538-545.
22. Wu, Z.; Chang, J.; Guo, X.; Niu, D.; Ren, A.; Li, P.; Zhou, H., Honeycomb-like bamboo powders-derived porous carbon with low filler loading, high-performance microwave absorption. *Carbon* **2023,** *215*, 118415.
23. Gao, F.; Qu, J.; Geng, C.; Shao, G.; Wu, M., Self-templating synthesis of nitrogen-decorated hierarchical porous carbon from shrimp shell for supercapacitors. *Journal of Materials Chemistry A* **2016,** *4* (19), 7445-7452.
24. Sun, B.; Yuan, Y.; Li, H.; Li, X.; Zhang, C.; Guo, F.; Liu, X.; Wang, K.; Zhao, X. S., Waste-cellulose-derived porous carbon adsorbents for methyl orange removal. *Chemical Engineering Journal* **2019,** *371*, 55-63.
25. Zhang, Z.; Cai, Z.; Wang, Z.; Peng, Y.; Xia, L.; Ma, S.; Yin, Z.; Huang, Y., A review on metal-organic framework-derived porous carbon-based novel microwave absorption materials. *Nano-Micro Letters* **2021,** *13* (1), 56.
26. Bai, T.; Guo, Y.; Liu, H.; Song, G.; Zhang, D.; Wang, Y.; Mi, L.; Guo, Z.; Liu, C.; Shen, C., Achieving enhanced electromagnetic shielding and absorption capacity of cellulose-derived carbon aerogels via tuning the carbonization temperature. *Journal of Materials Chemistry C* **2020,** *8* (15), 5191-5201.
27. Zhou, H. C.; Kitagawa, S., Metal-organic frameworks (MOFs). *Chemical Society Reviews* **2014,** *43* (16), 5415-5418.
28. McKinstry, C.; Cathcart, R. J.; Cussen, E. J.; Fletcher, A. J.; Patwardhan, S. V.; Sefcik, J., Scalable continuous solvothermal synthesis of metal organic

framework (MOF-5) crystals. *Chemical Engineering Journal* **2016,** *285*, 718-725.
29. Sheberla, D.; Sun, L.; Blood-Forsythe, M. A.; Er, S.; Wade, C. R.; Brozek, C. K.; Aspuru-Guzik, A.; Dinca, M., High electrical conductivity in Ni(3)(2,3,6,7,10,11-hexaiminotriphenylene)(2), a semiconducting metal-organic graphene analogue. *Journal of the American Chemical Society* **2014,** *136* (25), 8859-8862.
30. Chen, C.; Feng, X.; Zhu, Q.; Dong, R.; Yang, R.; Cheng, Y.; He, C., Microwave-assisted rapid synthesis of well-shaped MOF-74 (Ni) for CO2 efficient capture. *Inorganic Chemistry* **2019,** *58* (4), 2717-2728.
31. Yu, K.; Lee, Y.-R.; Seo, J. Y.; Baek, K.-Y.; Chung, Y.-M.; Ahn, W.-S., Sonochemical synthesis of Zr-based porphyrinic MOF-525 and MOF-545: Enhancement in catalytic and adsorption properties. *Microporous and Mesoporous Materials* **2021,** *316*, 110985.
32. Chen, Y.; Wu, H.; Liu, Z.; Sun, X.; Xia, Q.; Li, Z., Liquid-assisted mechanochemical synthesis of copper based MOF-505 for the separation of CO2 over CH4 or N2. *Industrial & Engineering Chemistry Research* **2018,** *57* (2), 703-709.
33. Furukawa, H.; Ko, N.; Go, Y. B.; Aratani, N.; Choi, S. B.; Choi, E.; Yazaydin, A. Ö.; Snurr, R. Q.; O'Keeffe, M.; Kim, J.; Yaghi, O. M., Ultrahigh porosity in metal-organic frameworks. *Science* **2010,** *329* (5990), 424-428.
34. Daglar, H.; Gulbalkan, H. C.; Avci, G.; Aksu, G. O.; Altundal, O. F.; Altintas, C.; Erucar, I.; Keskin, S., Effect of metal–organic framework (MOF) Database selection on the assessment of gas storage and separation potentials of MOFs. *Angewandte Chemie International Edition* **2021,** *60* (14), 7828-7837.
35. Zhong, Y.; Liao, P.; Kang, J.; Liu, Q.; Wang, S.; Li, S.; Liu, X.; Li, G., Locking effect in Metal@MOF with superior stability for highly chemoselective catalysis. *Journal of the American Chemical Society* **2023,** *145* (8), 4659-4666.
36. Yin, Y.; Yang, J.; Pan, Y.; Gao, Y.; Huang, L.; Luan, X.; Lin, Z.; Zhu, W.; Li, Y.; Song, Y., Mesopore to macropore transformation of metal–organic framework for drug delivery in inflammatory bowel disease. *Advanced Healthcare Materials* **2021,** *10* (3), 2000973.
37. Wang, X.; Zhang, X.; Zhao, Y.; Luo, D.; Shui, L.; Li, Y.; Ma, G.; Zhu, Y.; Zhang, Y.; Zhou, G.; Yu, A.; Chen, Z., Accelerated multi-step sulfur redox reactions in lithium-sulfur batteries enabled by dual defects in metal-organic framework-based catalysts. *Angewandte Chemie International Edition* **2023,** *62* (42), e202306901.
38. Ye, Y.; Gong, L.; Xiang, S.; Zhang, Z.; Chen, B., Metal–organic frameworks as a versatile platform for proton conductors. *Advanced Materials* **2020,** *32* (21), 1907090.
39. Xu, H.; Zhong, F.; Chen, F.; Luan, T.-X.; Li, P.; Xu, S.; Gao, J., A Zr-MOF nanoflower sensor and its mixed-matrix membrane for the highly sensitive detection of nitroaromatics. *Journal of Materials Chemistry C* **2022,** *10* (19), 7469-7475.
40. Hmadeh, M.; Lu, Z.; Liu, Z.; Gándara, F.; Furukawa, H.; Wan, S.; Augustyn, V.; Chang, R.; Liao, L.; Zhou, F.; Perre, E.; Ozolins, V.; Suenaga, K.; Duan, X.; Dunn, B.; Yamamto, Y.; Terasaki, O.; Yaghi, O. M., New porous crystals of extended metal-catecholates. *Chemistry of Materials* **2012,** *24* (18), 3511-3513.
41. Park, J.; Lee, M.; Feng, D.; Huang, Z.; Hinckley, A. C.; Yakovenko, A.; Zou, X.; Cui, Y.; Bao, Z., Stabilization of hexaaminobenzene in a 2D conductive

metal-organic framework for high power sodium storage. *Journal of the American Chemical Society* **2018,** *140* (32), 10315-10323.
42. Rubio-Gimenez, V.; Arnauts, G.; Wang, M.; Oliveros Mata, E. S.; Huang, X.; Lan, T.; Tietze, M. L.; Kravchenko, D. E.; Smets, J.; Wauteraerts, N.; Khadiev, A.; Novikov, D. V.; Makarov, D.; Dong, R.; Ameloot, R., Chemical vapor deposition and high-resolution patterning of a highly conductive two-dimensional coordination polymer film. *Journal of the American Chemical Society* **2023,** *145* (1), 152-159.
43. Li, W.-H.; Deng, W.-H.; Wang, G.-E.; Xu, G., Conductive MOFs. *EnergyChem* **2020,** *2* (2), 100029.
44. Xie, L. S.; Skorupskii, G.; Dinca, M., Electrically conductive metal-organic frameworks. *Chemical Reviews* **2020,** *120* (16), 8536-8580.
45. Sheberla, D.; Bachman, J. C.; Elias, J. S.; Sun, C. J.; Shao-Horn, Y.; Dinca, M., Conductive MOF electrodes for stable supercapacitors with high areal capacitance. *Nature Materials* **2017,** *16* (2), 220-224.
46. Feng, D.; Lei, T.; Lukatskaya, M. R.; Park, J.; Huang, Z.; Lee, M.; Shaw, L.; Chen, S.; Yakovenko, A. A.; Kulkarni, A.; Xiao, J.; Fredrickson, K.; Tok, J. B.; Zou, X.; Cui, Y.; Bao, Z., Robust and conductive two-dimensional metal−organic frameworks with exceptionally high volumetric and areal capacitance. *Nature Energy* **2018,** *3* (1), 30-36.
47. Smith, M. K.; Mirica, K. A., Self-organized frameworks on textiles (SOFT): conductive fabrics for simultaneous sensing, capture, and filtration of gases. *Journal of the American Chemical Society* **2017,** *139* (46), 16759-16767.
48. Zang, Y.; Pei, F.; Huang, J.; Fu, Z.; Xu, G.; Fang, X., Large-area preparation of crack-free crystalline microporous conductive membrane to upgrade high energy lithium–sulfur batteries. *Advanced Energy Materials* **2018,** *8* (31), 1802052.
49. Tan, K. T.; Ghosh, S.; Wang, Z.; Wen, F.; Rodríguez-San-Miguel, D.; Feng, J.; Huang, N.; Wang, W.; Zamora, F.; Feng, X.; Thomas, A.; Jiang, D., Covalent organic frameworks. *Nature Reviews Methods Primers* **2023,** *3*,1.
50. Zhang, P.; Wang, Z.; Wang, S.; Wang, J.; Liu, J.; Wang, T.; Chen, Y.; Cheng, P.; Zhang, Z., Fabricating industry-compatible olefin-linked COF resins for oxoanion pollutant scavenging. *Angewandte Chemie International Edition* **2022,** *61* (52), e202213247.
51. Sun, T.; Liang, Y.; Luo, W.; Zhang, L.; Cao, X.; Xu, Y., A general strategy for kilogram-scale preparation of highly crystalline covalent triazine frameworks. *Angewandte Chemie International Edition* **2022,** *61* (25), e202203327.
52. Zhang, M.; Li, L.; Lin, Q.; Tang, M.; Wu, Y.; Ke, C., Hierarchical-coassembly-enabled 3D-printing of homogeneous and heterogeneous covalent organic frameworks. *Journal of the American Chemical Society* **2019,** *141* (13), 5154-5158.
53. Zhao, X.; Pachfule, P.; Li, S.; Langenhahn, T.; Ye, M.; Schlesiger, C.; Praetz, S.; Schmidt, J.; Thomas, A., Macro/microporous covalent organic frameworks for efficient electrocatalysis. *Journal of the American Chemical Society* **2019,** *141* (16), 6623-6630.
54. Kandambeth, S.; Biswal, B. P.; Chaudhari, H. D.; Rout, K. C.; Kunjattu, H. S.; Mitra, S.; Karak, S.; Das, A.; Mukherjee, R.; Kharul, U. K.; Banerjee, R., Selective molecular sieving in self-standing porous covalent-organic-framework membranes. *Advance Materials* **2017,** *29* (2), 1603945.
55. Yang, M.; Hanayama, H.; Fang, L.; Addicoat, M. A.; Guo, Y.; Graf, R.; Harano, K.; Kikkawa, J.; Jin, E.; Narita, A.; Mullen, K., Saturated linkers in

two-dimensional covalent organic frameworks boost their luminescence. *Journal of the American Chemical Society* **2023,** *145* (26), 14417-14426.
56. Chen, Y. J.; Liu, M.; Chen, J.; Huang, X.; Li, Q. H.; Ye, X. L.; Wang, G. E.; Xu, G., Dangling bond formation on COF nanosheets for enhancing sensing performances. *Chemical Science* **2023,** *14* (18), 4824-4831.
57. Ding, C.; Breunig, M.; Timm, J.; Marschall, R.; Senker, J.; Agarwal, S., Flexible, mechanically stable, porous self-standing microfiber network membranes of covalent organic frameworks: preparation method and characterization. *Advanced Functional Materials* **2021,** *31* (49), 2106507.
58. Xia, Z. J.; Yang, H. C.; Chen, Z.; Waldman, R. Z.; Zhao, Y.; Zhang, C.; Patel, S. N.; Darling, S. B., Porphyrin covalent organic framework (POF)-based interface engineering for solar steam generation. *Advanced Materials Interfaces* **2019,** *6* (11), 1900254.
59. Ding, S. Y.; Gao, J.; Wang, Q.; Zhang, Y.; Song, W. G.; Su, C. Y.; Wang, W., Construction of covalent organic framework for catalysis: Pd/COF-LZU1 in Suzuki-Miyaura coupling reaction. *Journal of the American Chemical Society* **2011,** *133* (49), 19816-19822.
60. Uribe-Romo, F. J.; Hunt, J. R.; Furukawa, H.; Klöck, C.; O'Keeffe, M.; Yaghi, O. M., A crystalline imine-linked 3-D porous covalent organic framework. *Journal of the American Chemical Society* **2009,** *131* (13), 4570-4571.
61. Pang, Z. F.; Xu, S. Q.; Zhou, T. Y.; Liang, R. R.; Zhan, T. G.; Zhao, X., Construction of covalent organic frameworks bearing three different kinds of pores through the heterostructural mixed linker strategy. *Journal of the American Chemical Society* **2016,** *138* (14), 4710-4713.
62. Zhao, W.; Yan, P.; Yang, H.; Bahri, M.; James, A. M.; Chen, H.; Liu, L.; Li, B.; Pang, Z.; Clowes, R.; Browning, N. D.; Ward, J. W.; Wu, Y.; Cooper, A. I., Using sound to synthesize covalent organic frameworks in water. *Nature Synthesis* **2022,** *1* (1), 87-95.
63. Zhang, C.; Mo, J.; Fu, Q.; Liu, Y.; Wang, S.; Nie, S., Wood-cellulose-fiber-based functional materials for triboelectric nanogenerators. *Nano Energy* **2021,** *81,* 105637.
64. Wu, Z. Y.; Liang, H. W.; Chen, L. F.; Hu, B. C.; Yu, S. H., Bacterial cellulose: a robust platform for design of three dimensional carbon-based functional nanomaterials. *Accounts of Chemical Research* **2016,** *49* (1), 96-105.
65. Mihranyan, A., Cellulose from cladophorales green algae: From environmental problem to high-tech composite materials. *Journal of Applied Polymer Science* **2010,** *119* (4), 2449-2460.
66. Wang, Y.; Zhang, J.; Wang, X.; Zhang, T.; Zhang, F.; Zhang, S.; Li, Y.; Gao, W.; You, C.; Wang, X.; Yu, K., Cellulose nanofibers extracted from natural wood improve the postharvest appearance quality of apples. *Frontiers in Nutrition* **2022,** *9*, 881783.
67. Zhao, D.; Zhu, Y.; Cheng, W.; Chen, W.; Wu, Y.; Yu, H., Cellulose-based flexible functional materials for emerging intelligent electronics. *Advance Materials* **2021,** *33* (28), e2000619.
68. Zhuo, H.; Hu, Y.; Chen, Z.; Zhong, L., Cellulose carbon aerogel/PPy composites for high-performance supercapacitor. *Carbohydrate Polymers* **2019,** *215*, 322-329.
69. Quellmalz, A.; Mihranyan, A., Citric acid cross-linked nanocellulose-based paper for size-exclusion nanofiltration. *ACS Biomaterials Science & Engineering* **2015,** *1* (4), 271-276.
70. Tajima, K.; Imai, T.; Yui, T.; Yao, M.; Saxena, I., Cellulose-synthesizing machinery in bacteria. *Cellulose* **2021,** *29* (5), 2755-2777.

71. Zhou, S.; Kong, X.; Zheng, B.; Huo, F.; Stromme, M.; Xu, C., Cellulose nanofiber @ conductive metal-organic frameworks for high-performance flexible supercapacitors. *ACS Nano* **2019,** *13* (8), 9578-9586.
72. Favier, V.; Chanzy, H.; and Cavaille, J. Y., Polymer nanocomposites reinforced by cellulose whiskers. *Macromolecules* **1995**, 28, 6365-6367.
73. Iwamoto, S.; Lee, S.-H.; Endo, T., Relationship between aspect ratio and suspension viscosity of wood cellulose nanofibers. *Polymer Journal* **2013,** *46* (1), 73-76.
74. Sehaqui, H.; Zhou, Q.; Ikkala, O.; Berglund, L. A., Strong and tough cellulose nanopaper with high specific surface area and porosity. *Biomacromolecules* **2011,** *12* (10), 3638-3644.
75. Nogi, M.; Iwamoto, S.; Nakagaito, A. N.; Yano, H., Optically transparent nanofiber paper. *Advanced Materials* **2009,** *21* (16), 1595-1598.
76. Lin, S.-P.; Loira Calvar, I.; Catchmark, J. M.; Liu, J.-R.; Demirci, A.; Cheng, K.-C., Biosynthesis, production and applications of bacterial cellulose. *Cellulose* **2013,** *20* (5), 2191-2219.
77. Heßler, N.; Klemm, D., Alteration of bacterial nanocellulose structure by in situ modification using polyethylene glycol and carbohydrate additives. *Cellulose* **2009,** *16* (5), 899-910.
78. Kalashnikova, I.; Bizot, H.; Bertoncini, P.; Cathala, B.; Capron, I., Cellulosic nanorods of various aspect ratios for oil in water Pickering emulsions. *Soft Matter* **2013,** *9* (3), 952-959.
79. Mihranyan, A.; Llagostera, A. P.; Karmhag, R.; Stromme, M.; Ek, R., Moisture sorption by cellulose powders of varying crystallinity. *International Journal of Pharmaceutics* **2004,** *269* (2), 433-442.
80. Yousefi, H.; Azad, S.; Mashkour, M.; Khazaeian, A., Cellulose nanofiber board. *Carbohydrate Polymer* **2018,** *187*, 133-139.
81. Gustafsson, S.; Lordat, P.; Hanrieder, T.; Asper, M.; Schaefer, O.; Mihranyan, A., Mille-feuille paper: a novel type of filter architecture for advanced virus separation applications. *Materials Horizons* **2016,** *3* (4), 320-327.
82. Cho, S. Y.; Yu, H.; Choi, J.; Kang, H.; Park, S.; Jang, J. S.; Hong, H. J.; Kim, I. D.; Lee, S. K.; Jeong, H. S.; Jung, H. T., Continuous meter-scale synthesis of weavable tunicate cellulose/carbon nanotube fibers for high-performance wearable sensors. *ACS Nano* **2019**, 13 (8), 9332-9341.
83. Wu, H.; Zhang, Y.; Yuan, W.; Zhao, Y.; Luo, S.; Yuan, X.; Zheng, L.; Cheng, L., Highly flexible, foldable and stretchable Ni–Co layered double hydroxide/polyaniline/bacterial cellulose electrodes for high-performance all-solid-state supercapacitors. *Journal of Materials Chemistry A* **2018,** *6* (34), 16617-16626.
84. Wang, Z.; Carlsson, D. O.; Tammela, P.; Hua, K.; Zhang, P.; Nyholm, L.; Strømme, M., Surface modified nanocellulose fibers yield conducting polymer-based flexible supercapacitors with enhanced capacitances. *ACS Nano* **2015,** *9* (7), 7563-7571.
85. Zhou, S.; Apostolopoulou-Kalkavoura, V.; Tavares da Costa, M. V.; Bergstrom, L.; Stromme, M.; Xu, C., Elastic Aerogels of Cellulose nanofibers@metal-organic frameworks for thermal insulation and fire retardancy. *Nano-Micro Letters* **2019,** *12* (1), 9.
86. Kong, X.; Wu, Z.; Stromme, M.; Xu, C., Ambient aqueous synthesis of imine-linked covalent organic frameworks (COFs) and fabrication of freestanding cellulose nanofiber@COF nanopapers. *Journal of the American Chemical Society* **2024,** *146*, 742-751.

87. Kong, X.; Zhou, S.; Strømme, M.; Xu, C., All-cellulose-based freestanding porous carbon nanocomposites and their versatile applications. *Composites Part B: Engineering* **2022,** *232,* 109602.
88. Kong, X.; Zhou, S.; Strømme, M.; Xu, C., Redox active covalent organic framework-based conductive nanofibers for flexible energy storage device. *Carbon* **2021,** *171*, 248-256.
89. DeBlase, C. R.; Silberstein, K. E.; Truong, T. T.; Abruna, H. D.; Dichtel, W. R., beta-Ketoenamine-linked covalent organic frameworks capable of pseudocapacitive energy storage. *Journal of the American Chemical Society* **2013,** *135* (45), 16821-16824.
90. Zhao, W.; Yan, P.; Li, B.; Bahri, M.; Liu, L.; Zhou, X.; Clowes, R.; Browning, N. D.; Wu, Y.; Ward, J. W.; Cooper, A. I., Accelerated synthesis and discovery of covalent organic framework photocatalysts for hydrogen peroxide production. *Journal of the American Chemical Society* **2022,** *144* (22), 9902-9909.
91. Zhang, F.; Zhang, J.; Zhang, B.; Tan, X.; Shao, D.; Shi, J.; Tan, D.; Liu, L.; Feng, J.; Han, B.; Yang, G.; Zheng, L.; Zhang, J., Room-temperature synthesis of covalent organic framework (COF-LZU1) nanobars in CO(2) /water solvent. *ChemSusChem* **2018,** *11* (20), 3576-3580.
92. Ma, T.; Kapustin, E. A.; Yin, S. X.; Liang, L.; Zhou, Z.; Niu, J.; Li, L.-H.; Wang, Y.; Su, J.; Li, J.; Wang, X.; Wang, W. D.; Wang, W.; Sun, J.; Yaghi, O. M., Single-crystal x-ray diffraction structures of covalent organic frameworks. *Science* **2018,** *361* (6397), 48-52.
93. Sultan, S.; Abdelhamid, H. N.; Zou, X.; Mathew, A. P., CelloMOF: nanocellulose enabled 3D printing of metal–organic frameworks. *Advanced Functional Materials* **2018,** *29* (2), 1805372.
94. Liu, Y.; Wei, Y.; Liu, M.; Bai, Y.; Wang, X.; Shang, S.; Du, C.; Gao, W.; Chen, J.; Liu, Y., Face-to-face growth of wafer-scale 2d semiconducting mof films on dielectric substrates. *Advance Materials* **2021,** *33* (13), e2007741.
95. Yan, X.; Lyu, S.; Xu, X. Q.; Chen, W.; Shang, P.; Yang, Z.; Zhang, G.; Chen, W.; Wang, Y.; Chen, L., Superhydrophilic 2D Covalent Organic Frameworks as Broadband Absorbers for Efficient Solar Steam Generation. *Angewandte Chemie International Edition* **2022,** *61* (19), e202201900.
96. Zhou, S.; Kong, X.; Strømme, M.; Xu, C., Efficient solar thermal energy conversion and utilization by a film of conductive metal–organic framework layered on nanocellulose. *ACS Materials Letters* **2022,** *4* (6), 1058-1064.

Acta Universitatis Upsaliensis

Digital Comprehensive Summaries of Uppsala Dissertations from the Faculty of Science and Technology 2399

Editor: The Dean of the Faculty of Science and Technology

A doctoral dissertation from the Faculty of Science and Technology, Uppsala University, is usually a summary of a number of papers. A few copies of the complete dissertation are kept at major Swedish research libraries, while the summary alone is distributed internationally through the series Digital Comprehensive Summaries of Uppsala Dissertations from the Faculty of Science and Technology. (Prior to January, 2005, the series was published under the title "Comprehensive Summaries of Uppsala Dissertations from the Faculty of Science and Technology".)

Distribution: publications.uu.se
urn:nbn:se:uu:diva-526314

ACTA UNIVERSITATIS
UPSALIENSIS
2024